UNIVERSITY OF ZULULAND

Synthesis and Fabrication of Alpha Phase Iron Oxide (α-Fe_2O_3) Nanostructured doped with Ruthenium for Highly Sensitive and Selective Flammable and Toxic Gas Sensor

Dissertation submitted in partial-fulfilment of the requirements for the degree of Master of Science to the:

Faculty of Science, Agriculture and Engineering

Department of Physics

UNIVERSITY OF ZULULAND

Supervisors: Dr. C.L. Ndlangamandla

Co-Supervisor: Dr S.S Nkosi

Submitted by

NG Cebekhulu

Declaration

This dissertation, written by Ntokozo God-knowledge Cebekhulu, is an original piece that has not been sent to any other South African university.

Signature ……  ……..

Date……30/12/ 2022…….

Dedication

This work is dedicated to my lovely family.

Acknowledgment

- I would like to thank God who keeps me alive and protects me and gives me the strength to stand through all the difficult times.
- I would like to thank my loved family for supporting me all the time.
- I would like to thank my supervisors Dr. CL Ndlangamandla and Dr. SS Nkosi for encouraging and guiding me through this work.
- I would like to thank the National Research Foundation (NRF) for its finances.
- I like to thank Mr. Mailman, Mr. Masikane, and Thulani Shabangu from the Department of Chemistry at the University of Zululand for helping with X-ray diffraction (XRD).
- I would thank Dr. Solly Motaung and Thomas Malwela for helping me with the data of BET and TGA at CSIR.
- I would like to thank the UKZN team for helping me with SEM and HRTEM.
- I would like to thank the UFS team for helping me with the XPS data.
- I would to thank Mrs. N.C. Mothapo for being supportive and kind whenever I needed assistance with printing.
- I would like to thank all my friends in and out of the academic field for their support.
- Finally, thanks to all the staff members and my fellow research students in the Department of Physics at the University of Zululand.

Abstract

The increase in the number of manufacturing industries in recent times had both positive and negative impacts on our environment and human health. The use of heavy-duty machines in manufacturing industries causes the release of flammable and hazardous gases, which affect human health, into the atmosphere. Many research efforts have been focused on detecting and monitoring these gases using metal oxide semiconductor materials. This study investigates the gas sensing performance of ruthenium-doped alpha iron oxide towards flammable and hazardous gases. The chemical precipitation method synthesised the alpha iron oxide doped with a different weight percentage of ruthenium. The samples underwent some characterisation techniques, such as X-ray diffractometry, thermogravimetric analysis, x-ray photoelectron spectroscopy, Brunauer-emmett-teller surface area analysis, scanning electron microscopy, and high-resolution transmission electron microscopy, to study certain properties of the material. The sensors were fabricated by using the drop-casting method, and the sensors were tested for gas sensing performance at 225 ºC operating temperature, towards liquefied petroleum gas (LPG), ethanol, propanol, ammonium (NH_3), and hydrogen sulphide (H_2S). The pure sample alpha iron oxide (α-Fe_2O_3) was more sensitive to the target gases with the response being 26.01 towards the ammonia gas. The selectivity shift towards LPG while the response decreases upon the addition of different weight percentage of the ruthenium to alpha iron oxide ruthenium was found to be unsuitable as a dopant material in alpha iron oxide for gas sensing applications.

Keywords: Gas sensing, Ru, α-Fe_2O_3-based sensor, Sensitivity, Flammable gases.

List of Abbreviations

NIOSH	National Institute for Occupational Safety and Health
IDLH	Immediately Dangerous to Life or Health
Ru	Ruthenium (dopant material)
LPG	Liquefied Petroleum Gas
RH	Relativity Humidity
H_2	Hydrogen
XRD	X-Ray Diffraction
XPS	X- Ray Photoelectron Spectroscopy
HR-TEM	High- Resolution Transmission Electron Microscopy
SEM	Scanning Electron Microscopy
TGA	Thermogravimetric Analysis
BET	Brunauer- Emmett-Teller
CO	Carbon Monoxide
NO_2	Nitrogen Dioxide
VOCs	Volatile Organic Compounds
HPLC	Highly Performance Liquid Chromatography
GC/ MS	Gas Chromatography/ Mass Spectrometry
MOS	Metal Oxide Semiconductors
WHO	World Health Organization
TLVs	Threshold Limit Value
NH_4OH	Ammonia Hydroxide
SSA	Specific Surface Area
SAED	Selected Area Electron Diffractions
$FeCl_3.H_2O$	Iron (Ⅲ) Chloride hex hydrate
α-Fe_2O_3	Hematite (Alpha phase iron oxide)
Fe_2O_3	Iron (Ⅲ) oxide

Table of Contents

List of Tables

List of Figures

Chapter 1

1 introduction

1.1 Air pollution

According to the World Health Organization (WHO), air pollution is one of the biggest problems the world is now experiencing. Any activity that changes the natural nature of the atmosphere, whether it is a chemical, physical, or biological, causes air pollution. The primary sources of air pollution are household combustion appliances, motor vehicles, industrial operations, and forest fires (see **Fig.1.1 &1.2**). Industrialisation is generally viewed as a good thing, but it comes with many challenges that ruin our environment. Pollutants emitted by industries, companies, and motor vehicles contribute to global warming and climate-related disaster and has a bad impart on agriculture **[1, 2]**. Every gas in the atmosphere has a threshold limit value (TLV), which is the highest concentration of the corresponding poisonous gas that people may breathe without getting sick. TLVs are expressed in parts per million (ppm) **[3]**. Indoor and outdoor air pollution are major contributors to morbidity and mortality as well as the formation of respiratory and other illnesses like lung cancer and asthma. Approximately 7 million people died from indoor and outdoor pollution in 2016, making it the fourth largest cause of death globally. Statistics from the World Health Organization (WHO) show that in 2016, air pollution alone was responsible for 4.2 million deaths, while household air pollution accounted for another 3.6 million **[4, 5]**. The greatest environmental threat to human health in 2019 was air pollution. Indoor air quality is similarly significant because humans spend most of their time indoors, such as in our homes, working place, schools, etc., where most combustible and hazardous gases, such as CO_2, CO, Benzene, and Toluene, are present. Therefore, it is essential to control air pollution both inside and outside **[6, 7].** Living in a clean and secure environment is essential for humans and other living things worldwide. Any gas leak into the environment or atmosphere would be dangerous to people's health **[3]**. Over the past decade, there has been a quest to monitor air pollution in our environment **[8]**. Almost all mammals and reptiles have a main olfactory system and an accessory olfactory system. The olfactory system is a special sense of smell that has a direct relationship with special organs. This can detect odorous gases such as

hydrogen sulphide and ammonia, and organic compounds (VOCs). Some of the hazardous gases such as carbon monoxide and hydrogen dioxide remain impossible to be detected by humans despite their excellent olfactory system since they are odourless, tasteless, and colourless **[8]**. Therefore, it is essential to develop equipment and manufacture a good sensor for early detection or alert of flammable, explosive, or toxic gases present in the environment **[9]**. Two methods have been developed for the detection of gases and VOCs, namely high-performance liquid chromatography (HPLC) and gas chromatography/mass spectrometry (GC/MS). However, these techniques can be expensive and time-consuming and, these days, the sample and convenient methods for the detection of gases like those mentioned above are in great demand **[10]**. Therefore, developing an affordable gas sensor that serves this purpose is seen as a significant achievement in the field of science. Gas sensors can be in the form of different materials based on their purpose for that moment. During the design and fabrication of the gas sensor there are three requirements needed to be taken into consideration, i.e., high sensitivity, fast response, and high selectivity **[11]**. There are various types of gas sensors, which include optical gas sensors **[12]**, gas surface-acoustic sensors **[13]**, and gas sensors with thermal conductivity **[14]**. The most investigated one is the metal oxide base gas sensor due to its simplicity, low cost, and ability to detect different gases including flammable and toxic gases **[15]**. Gas sensors are divided into two types, namely, portable gas sensors and fixed gas sensors, and are used to ensure safety in households and the working environment **[16].**

Figure 1.1: Air pollution in our environment.

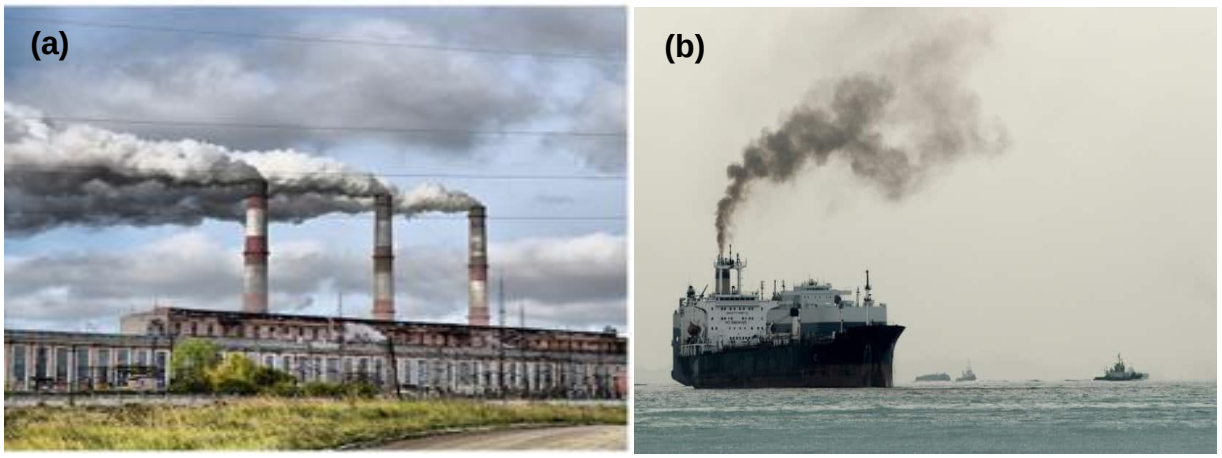

Figure 1.2: (a) Air pollution from industry and, (b) Air pollution from water vessels.

1.2 Problem statement and motivation

The detection of flammable, toxic, and hazardous gases, such as liquefied petroleum gas (LPG), hydrogen sulphide (H_2S), and ammonia (NH_3) gases remains a challenge. These gases are harmful to human health as they contribute to air pollution, climate change, and acid rain which badly impact agriculture, especially crop production. As these gases are harmful any exposure to them in high concentrations may lead to fatal health conditions. The detection and monitoring of toxic and flammable gases in the environment have been extensively investigated. Requirements for a good gas sensor are low operating temperature, detection below immediate danger to life or health concentrations, short response time, recovery times, high sensitivity, and selectivity.

1.3 Aim of the study

This study aimed to synthesise and fabricate an iron oxide (hematite) (α-Fe_2O_3) nanostructures-based gas sensor for the detection of flammable, toxic and hazardous gases. Ruthenium was used as a dopant to dope iron oxide nanostructures to investigate if the sensing properties of hematite (α-Fe_2O_3) nanostructure-based gas sensor is improved. The sensitivity (response and recovery time) and selectivity for the fabricated gas sensor towards the flammable and toxic gases were investigated.

1.4 Objectives

- To synthesise pure and doped hematite nanostructures using the chemical precipitation method and techniques such as powder x-ray diffraction (XRD), scanning electron microscopy (SEM), and High-resolution transmission electron microscopy (HR-TEM). Brunauer-emmett-teller (BET), X-ray photoelectron spectroscopy (XPS) and Thermogravimetric analysis (TGA) were used to characterise the as-synthesised samples.
- To fabricate hematite-based gas sensors by the drop-casting method.
- To test fabricated sensors towards flammable and toxic gases such as liquid petroleum gas (LPG), hydrogen sulphide (H_2S), ammonia (NH_3), propanol and ethanol at various operation temperatures (175^oC, 200^oC and 225^0C).

1.5 Dissertation outline

This section briefly outlines how the thesis is arranged. Chapter 1 is devoted to the introduction and motivation of the study. Chapter 2 is devoted to a literature review of both the material used and the history and the background of the gas sensors, while the methodology, synthesis, and experimental techniques used in this work are presented in chapter 3. The experimental procedure and results discussions are presented in chapter 4, while chapter 5 is about the conclusion and summary of the study. The recommendations and future plans are also included in this chapter.

Reference

1. Organization, W.H., *World health statistics 2015*. 2015: World Health Organization.
2. Organization, W.H., *World health statistics 2010*. 2010: World Health Organization.
3. Nkosi, S., et al., *The effect of stabilized ZnO nanostructures green luminescence towards LPG sensing capabilities.* Materials Chemistry and Physics, 2020. **242**: p. 122452.
4. Louis, D.N., et al., *The 2016 World Health Organization classification of tumors of the central nervous system: a summary.* Acta neuropathologica, 2016. **131**(6): p. 803-820.
5. Organization, W.H., *World health statistics 2016: monitoring health for the SDGs sustainable development goals*. 2016: World Health Organization.
6. Pandey, A., et al., *Health and economic impact of air pollution in the states of India: the Global Burden of Disease Study 2019.* The Lancet Planetary Health, 2021. **5**(1): p. e25-e38.
7. Fan, S.-J., et al., *Ambient air pollution and depression: a systematic review with meta-analysis up to 2019.* Science of The Total Environment, 2020. **701**: p. 134721.
8. Hijri, M., et al., *Al-doped ZnO for highly sensitive CO gas sensors.* Sensors and Actuators B: Chemical, 2014. **196**: p. 413-420.
9. Hoa, N.D., et al., *Meso-/nanoporous semiconducting metal oxides for gas sensor applications.* Journal of Nanomaterials, 2015. **2015**.
10. Cumalı, S. and K.C. Güven, *Air pollution of hydrocarbons exhausted from vehicles in tunnels, bridges of Istanbul and detection of 3-nitrophthalic in seawater near the side of boat.* Journal of Black Sea/Mediterranean Environment, 2007. **13**(2): p. 161-180.
11. Schütze, A., et al., *Highly sensitive and selective VOC sensor systems based on semiconductor gas sensors: how to?* Environments, 2017. **4**(1): p. 20.
12. Tavoli, F. and N. Alizadeh, *Optical ammonia gas sensor based on nanostructure dye-doped polypyrrole.* Sensors and Actuators B: Chemical, 2013. **176**: p. 761-767.

13. Jakubik, W.P., *Surface acoustic wave-based gas sensors.* Thin Solid Films, 2011. **520**(3): p. 986-993.
14. Tajima, K., et al., *Micromechanical fabrication of low-power thermoelectric hydrogen sensor.* Sensors and Actuators B: Chemical, 2005. **108**(1-2): p. 973-978.
15. Kim, T. and B. Guo, *Zn-doped γ-Fe2O3 sensors for flammable gas detection: Effect of annealing on sensitivity and stability.* Journal of Industrial and Engineering Chemistry, 2011. **17**(1): p. 158-164.
16. Guida, R. and B. Mandelli, *A portable gas recirculation unit for gaseous detectors.* Journal of Instrumentation, 2017. **12**(10): p. T10002.

Chapter 2

2. Literature review

2.1 Introduction

This chapter is devoted to providing background information on hematite nanostructures as gas sensor Nanostructured metal-oxide semiconductors (MOS) have attracted attention in recent years because of their distinct physical, chemical, and electrical properties when compared to bulk materials **[1]**. The most important aspects of this work are iron oxide (hematite) nanostructures, their structure, and their gas-sensing properties.

2.2. Metal oxide gas sensor

Gas sensors made of metal oxide semiconductors (MOS) are the most investigated type of sensors **[2]**. They are size-dependent, with their sizes ranging from 1 to 100 nm and are being used for gas detection. There are two types of semiconductors, namely, n-type and p-type. The electron dominates in n-type semiconductors, while holes dominate in p-type semiconductors. An n-type semiconductor has a much bigger electron density than a p-type semiconductor, which has a much larger hole density. An analysis of the metal oxide semiconductor reveals that, over time, n-type semiconductor oxides **[3]**, like tin oxide (SnO_2) **[4]**, zinc oxide (ZnO_2) **[5]**, titanium dioxide (TiO_2) **[6]**, tungsten oxide (WO_3) **[7]**, and hematite (α-Fe_2O_3) **[8]**, and, to a lesser degree, p-type semiconductor oxides such as CuO **[9],** NiO **[10]**, and Cr_2O_3 **[11]**, have been extensively studied as gas sensor materials. Complex (mixed metal) oxide has also been investigated **[12]**, such as perovskites **[13].** The focus has been always on the improvement of the sensing properties of this sensing material by doping or adding impurities to end up with sensing material such as Sr-doped Fe_2O_3 **[14]**, and Sn-doped $CoFe_2O_3$ **[15]**. There are several advantages of using metal oxide semiconductors as gas sensing material. These advantages are, low cost, easy fabrication, simplicity of use, and ability to detect different gases including flammable and toxic gases **[15]**.A metal oxide gas sensor operates on the chemo resistance concept, which involves a change in the thin film's electrical conductivity or resistivity as a result of exposure to a target gas **[16]**. Alternatively, gas molecules can interact

with the oxide by either giving or accepting charge carriers (receptor function) and alter metal oxide resistivity as shown in the **Fig.2.1** below.

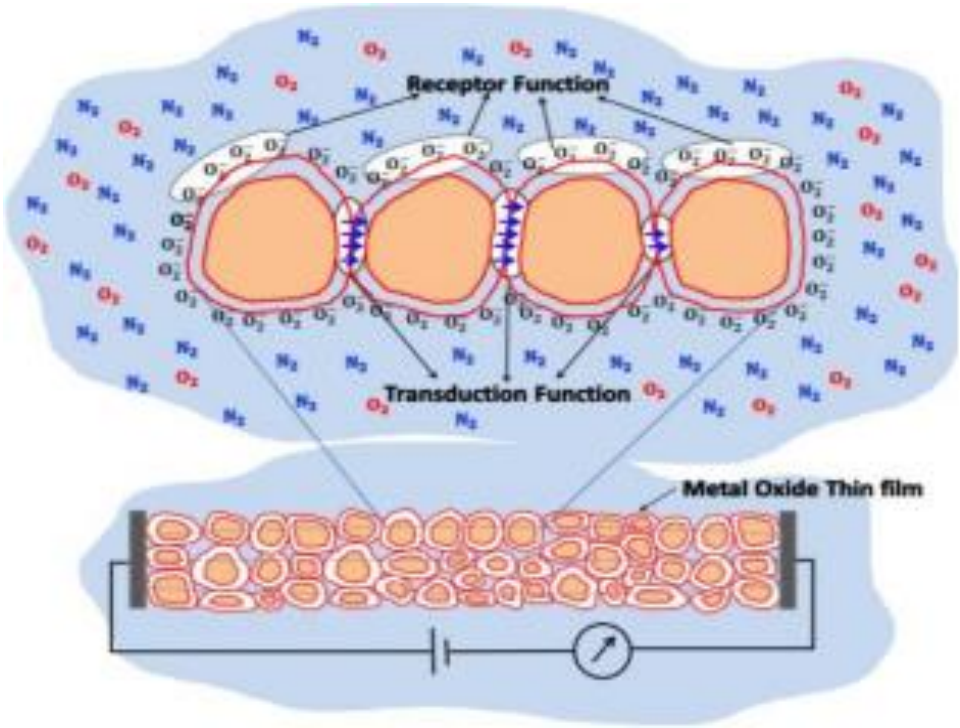

Figure 2.1: Schematic diagram of metal oxide thin film gas sensor **[16].**

2.3 Nanoparticles

Nanotechnology is the study of particles and materials with sizes ranging from 1 to 100 nm. Due to the increased molecular interaction, the particle can facilitate easy adsorption, absorption, and penetration. They have unique properties when compared with bulk materials, making them effective in research and development in different fields including medical, environmental, biomedical, electrical, and communication. Based on previous studies, it has been found that metal oxide nanoparticles can be used as a performance improver in engines. Nanoparticles can be produced either by biological or chemical methods **[17, 18]**. Among the many types of nanoparticles, metal nanoparticles - specifically iron oxide nanoparticles - hold a special position due to their super paramagnetic nature, small size, and wide range of applications **[19]**. Science and technology have long utilised nanostructured oxides as important nanomaterial. Over the past few decades, nanostructured metal oxides have attracted

considerable interest because they possess excellent properties and can be used in numerous areas, including catalysis, biomedicine, gas sensing, material chemistry, and electrochemistry.

2.4 Iron oxide

In the laboratory, iron oxide is an easily synthesised compound that is widespread. It is one of the most important transitional metal oxides for biology **[20]**. There are 16 pure forms of iron oxide. Iron oxides, hydroxides, and oxy-hydroxides are listed in **Table 1**. These compounds are interesting because of their trivalent state, low stability, and brilliant colour $Fe_8O_8(OH)(SO_4)\cdot nH_2O$ and $(Fe^{3+})_2O_3\cdot 0.5H_2O$ are poorly crystalline whereas all the rest of the iron oxides are crystalline **[21]**. Among the other oxides the three most common and studied are hematite (α-Fe_2O_3), maghemite (γ -Fe_2O_3), and magnetite (Fe_3O_4). Because of excellent photo corrosion resistance, low cost, and non-toxicity, the most thermodynamically stable iron oxide phase, α-Fe_2O_3, is of particular interest. It can also be used as a precursor to obtaining Fe_3O_4 or γ-Fe_2O_3. Furthermore, it is a semiconductor with a band gap of 2.1 eV **[22]**.

Table 1: Iron oxides, hydroxides, and oxy-hydroxides **[20]**.

Oxides	**Hydroxides**	**Oxy hydroxides**
FeO, iron(Ⅱ) oxide, (wustite)	iron(Ⅱ)hydroxide (Fe $(OH)_2$)	Goethite(α-FeOOH)
Fe_3O_4, iron (Ⅱ, Ⅲ) oxides (Magnetite)	iron(Ⅲ)hydroxides (Fe $(OH)_3$) (Bemalite)	Akagemeit (β- FeOOH)
Fe_2O_3, iron (Ⅲ) oxide		Lepidocrocite (γ- FeOOH)
α-Fe_2O_3, Hematite		Feroxyhyte (δ-FeOOH)
β- Fe_2O_3		Ferrihydrate, (Fe5HO8.4H2O Approx.)
γ- Fe_2O_3, Maghemite		
ε- Fe_2O_3		

Table 2: Properties of iron oxide **[20].**

Mineral	**Wustite**	**Magnetite**	**Maghemite**	**Hematite**
Formula	$Fe_{1-x}O$	Fe3O4	γ- Fe_2O_3,	α-Fe_2O_3
Cation	Fe^{2+}	Fe^{2+}/Fe^{3+}	Fe^{3+}	Fe^{3+}
Structural type	Defect rock salt	Inverse spinal	Defect spinal	Corundum
Crystallographic system	Cubic	Cubic	Cubic/tetragonal	Hexagonal
Space group	Fm3m	Fd 3m	$P4_332$	R3c
Anion stacking	FCC (111)	FCC (111)	FCC (111)	HCP (001)
Lattice Parameters (nm)	a= 0.4302-0.4275	a = 0.8396	a =0.83474	a = 0.50436 c =1.37489
Formula units/unit cell	4	8	8	6
Colour	Black	Black	Reddish-brown	Red
Density (gm^{1})	5.9-5.99	5.18	4.87	5.26
Mohs hardness	5	5	5.5	6.5
Melting point (ºC)	1377	1583-1597		1350
Boiling point (ºC)	2512	2623		
Magnetism	Antiferro-	Ferri	Ferri	Weak ferro/Anti-

Necl(curic) temperature (ºC)	203-211	850	820-986	956
The heat of Formation ($KJmo^{-1}$)	-251	-1012.6	-711.1	- 742.7

Atomic Radii

Fe (metallic) =0.126nm, O (covalent) = 0.066nm

Ironic Radii

Fe^{2+} = 0.082 nm, Fe^{3+} = 0.065 nm and O^{2-} = 0.14 nm

2.5 Crystalline structure of hematite

Hematite is a common choice for catalysis and gas sensors because of its low toxicity, high activity, and corrosion resistance **[23]**. It is very popular due to its application in the different fields of nanotechnology. Iron oxide-based nanostructures are popular in non-science and nanotechnology because of their size and shape-dependent physical and chemical characteristics **[24]**. Alpha iron oxide (α-Fe_2O_3) crystallises in a rhombohedra structure in which the Fe^{3+} ions are arranged in an octahedral geometry between two oxygen atoms and crystallise in the *R3C* space group **[25]**. With a lattice parameter of a = 0.50356 nm and c = 1.37489 nm, those atoms are grouped similarly to corundum structures. In the hematite structure, the anions O^{2-} are packed in a hexagonal closed-packed lattice that runs in the direction of [001]. (**Fig 2.2** and **2.3**) showing how the atoms are arranged in the crystalline structure; the green ball indicates the presence of the iron atom Fe^{3+} while the red ball is the oxygen atom.

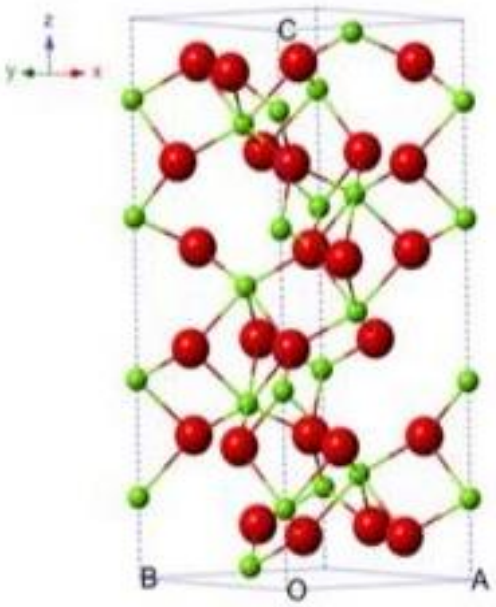

Figure 2.2: Hematite crystal structure (green ball is Fe^{3+} and the red ball is O^{2-}) **[24].**

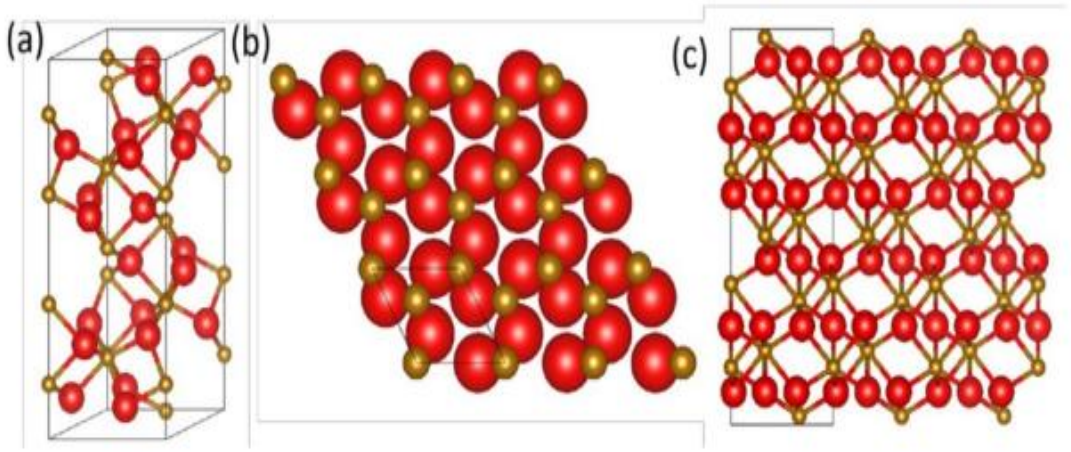

Figure 2.3: Hematite. (a) The hexagonal unit cell of α-Fe_2O_3 contains 6 formula units. O^{2-} anions are red, Fe^{3+}_{oct} cations are brown, and have the rhombohedra arrangement in the atoms. (b) Fe^{3+}_{oct} cations occupy two-thirds of the octahedral interstitial sites between hexagonal close-packed O^{2-} planes (drawn in space-filling style with unit cell indicated). (c) Shows the side view of the α-Fe_2O_3 structure that shows how the Fe^{3+}_{oct} cations are not coplanar **[24].**

2.6 Magnetic properties

The electronic configuration of Fe^{2+} consist of 24 electrons in the shell (Fe^{2+} = [Ar] 3d6, 4s) while the electronic configuration of Fe^{3+} have 23 electrons (Fe^{3+}= [Ar]3d5). Due to its 4 unpaired electrons in the 3d shell, iron exhibits a very strong magnetic field. Fe^{2+} iron has 4 unpaired electrons in the 3d shell, whereas Fe^{3+} iron has 5 unpaired electrons in the 3d shell. As a result, when iron atoms or Fe^{2+} and Fe^{3+} crystallise, they can be ferromagnetic, antiferromagnetic, or ferrimagnetic. This is shown in **Fig.2.4 (b-d).** When there are no magnetic fields, the magnetic moments of the atoms are randomly oriented in the paramagnetic state, and the substance has a zero net magnetic moment as shown in the **Fig.2.4 (a)**. When the applied fields are removed, the magnetic moment is zero. However, even in the absence of an external field, all the atomic moments in a ferromagnetic substance are aligned. A ferrimagnetic substance resembles a ferromagnetic material, but it contains two different types of atoms with opposing magnetic moments. The crystal is antiferromagnetic and has no net magnetic moment if its magnitudes are the same **[26].**

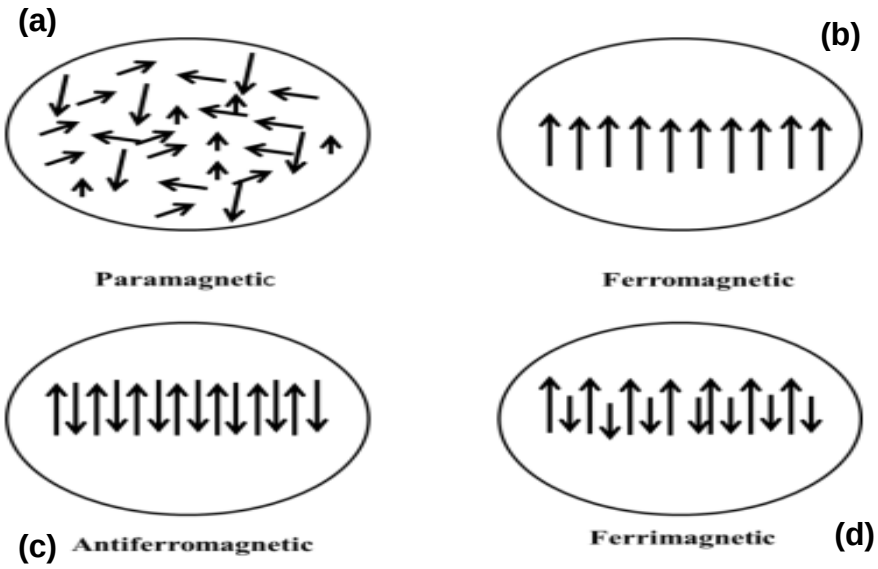

Figure 2.4: Alignment of individual atomic magnetic moment in various materials **[26].**

2.7 Band gap theory of semiconductors

When atoms come together, compounds are produced, and their orbital energy combines to generate molecular orbital energies. As a result of the increased atom mixing, the number of molecular orbitals generated has also increased. And all those energy levels are very close to each other. Those energy levels are forming a band of energy levels. According to the band theory a semiconductor behaves as insulation at absolute zero. If the temperature above this point is lower than the melting point of the solid, then the metal would act as a semiconductor. In the semiconductors, the valance band is fully occupied by the electron while the conduction band is being unoccupied this is represented in **Fig. 2.5,** and the bands have small gaps in between them. To move the electron from the valance band to the conduction band requires energy. The electron creates the hole in the valance band (VB) while is promoted to conduction band (CD), the hole mainly in the valance bands will behave as particles with a certain effective mass. While the band energy at the conduction band is approximately (E = 2.2 eV) **[26].**

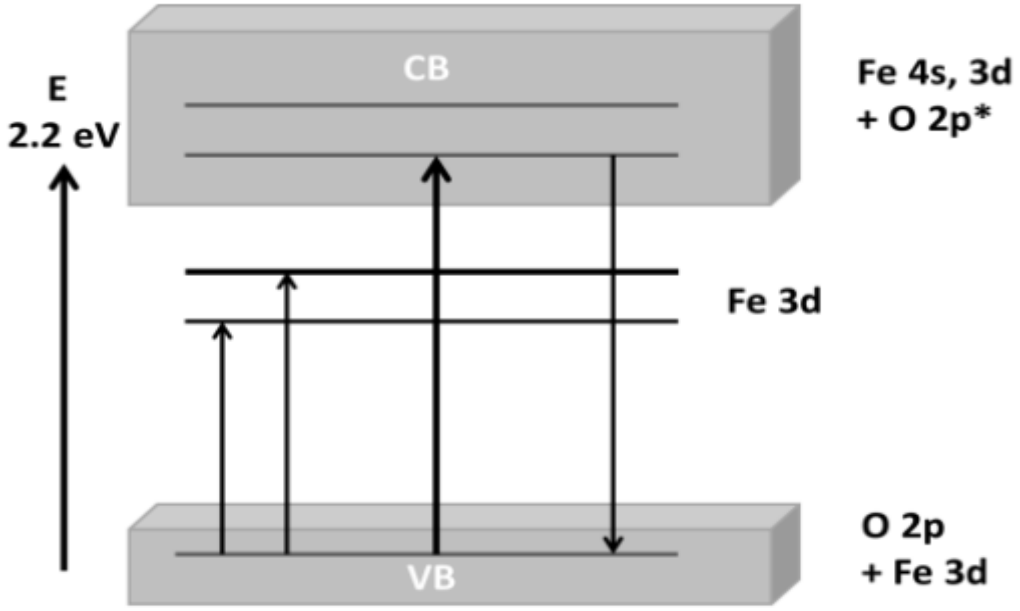

Figure 2.5: Schematic illustration of the electronic band structure of iron oxides (Fe^{3+}) **[26].**

2.8 Iron oxide as sensing material

As the demand for monitoring gaseous molecules in various applications grows, chemical and gas sensors are becoming more common around the world. For gas sensing applications, metal oxides with large band gap regions, such as SnO_2, TiO_2, ZnO, In_2O_3, Fe_2O_3, and WO_3, have been synthesised **[27]**. Metal oxides with a three-dimensional arrangement and porous structure, such as Fe_2O_3, have recently attracted a lot of interest for new applications. Fe_2O_3, a transition metal oxide that occurs naturally, is harmless, stable, and environmentally friendly **[28]**. This compound has been used to detect a range of gases, especially carbon monoxide (CO), xylene **[29]**, and acetone **[30]** among others.

2.9 Gas sensing characteristics

The fundamentals of operation of gas sensors are explained in terms of their principles of operation. The resistance variation on the electrode of the resistive sensor must be measured when the target gas is introduced. If the gas is exposed, the resistance normally varies according to the type of semiconductor or interaction with the dominant carrier. **Table 3** shows the sensor reactions of n-types and p-types material to oxidation or reducing gas **[31]**.

Table 3: Metal oxide semiconductor (MOS) when exposed to specific oxidizing and reducing gases **[31].**

Sensor-response behaviour	**n-types (MOS)**	**p-type MOS**	**Example of a target analyte.**
Oxidising gas	Resistance increasing	Resistance decreasing	O_2 ,O_3 ,CO_2 ,SO_2
Reducing gas	Resistance decreasing	Resistance increasing	H_2, H_2S, CO, NH_3, Ethanol, acetone, CH_4
Dominant-charger carrier	Electron (e^-)	Hole (h^+)	

When exposed to oxidising gases, MOSs gas sensors are affected because the gas interacts with oxygen ions in the environment and retains electrons as shown in **Table 3**. Because electrons are most charger transporters in MOSs, there is a reduction in the electron concentration. The electron concentration is reduced, however, because oxidising gas reduces the conductance of n-type MOSs. The majority of charge carriers in the p-types MOSs are the holes, which means that the resistance of the sensor will be decreasing while the operating temperature is being increased. However, under the oxygen ambient, p-types MOSs generate the holes when the oxygen ions are being adsorbed on the surface via the excited electron from the valance band to the conduction bands. In this case, the number of the charge carrier increases, which leads to decreases in the sensor resistance (opposite to n-types).

But if the p-type MOSs sensor is under the target gas ambient (Reducing gas), the electron is injected into the valance band, and they can recombine with the holes. This method results in reducing the number of holes, which leads to an increase in the sensor resistance which is also opposite to n-types. **Fig. 2.6 (a-b)** shows how the n-types and p-types play a role in the sensor response, and this shows how different types of semiconductors behaves.

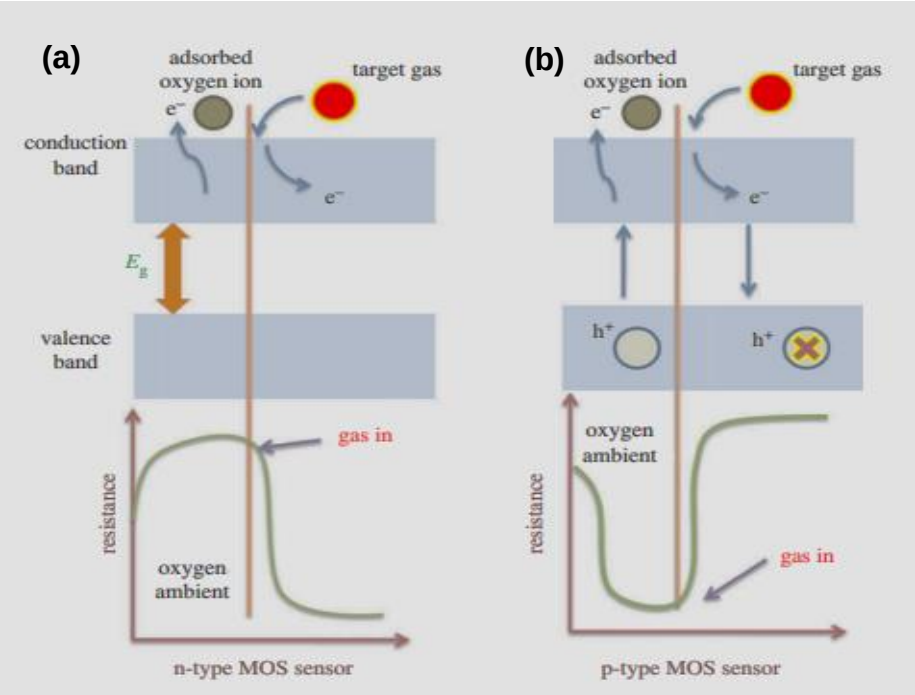

Figure 2.6: The sensing mechanisms of (a) n-type and (b) p-type MOSs **[32]**

2.10 Hematite gas sensing mechanism

Whenever n-type semiconductors like hematite and graphite are exposed to the gas, electron-depletion layers occur, and electrons are returned to the conduction band. In the beginning, the oxygen molecules from the air pass through the surface of the hematite and are adsorbed to the surface as shown in **reaction 2.1 [33]**.

$$O_{2\ (gas)} \rightarrow O_{2\ (ads).} \qquad (2.1)$$

Following this, the oxygen-free electrons form oxygen ions on the hematite surface with trapped electrons, as indicated in the following chemical reactions, which happen at temperatures below 100ºC **[34]**.

$$O_{2\,(ads)} + e^- \rightarrow O_2^-{}_{(ads)}\ (T< 100^oC), \qquad (2.2)$$

$$O_{2\,(ads)} + e^- \rightarrow 2O^-{}_{(ads)}\ (100^oC < T<300^oC), \qquad (2.3)$$

$$O^-{}_{(ads)}) + e^- \rightarrow O^{2-}{}_{ads}\ (T> 300^oC). \qquad (2.4)$$

The formation of an electron depletion layer on the layer of alpha iron oxide (α-Fe_2O_3) nanomaterial causes a decrease in carrier concentration and an increase in resistance. The Fermi level and conductor band are depicted in Fig. 2.7(b). The band of energy it emits in the air is shown in Fig. 2.7(c). Once the sensor is exposed to a vacuum, the energy band reaches a flat-band condition, as no electrons are transferred on the surface, as opposed to other environments.

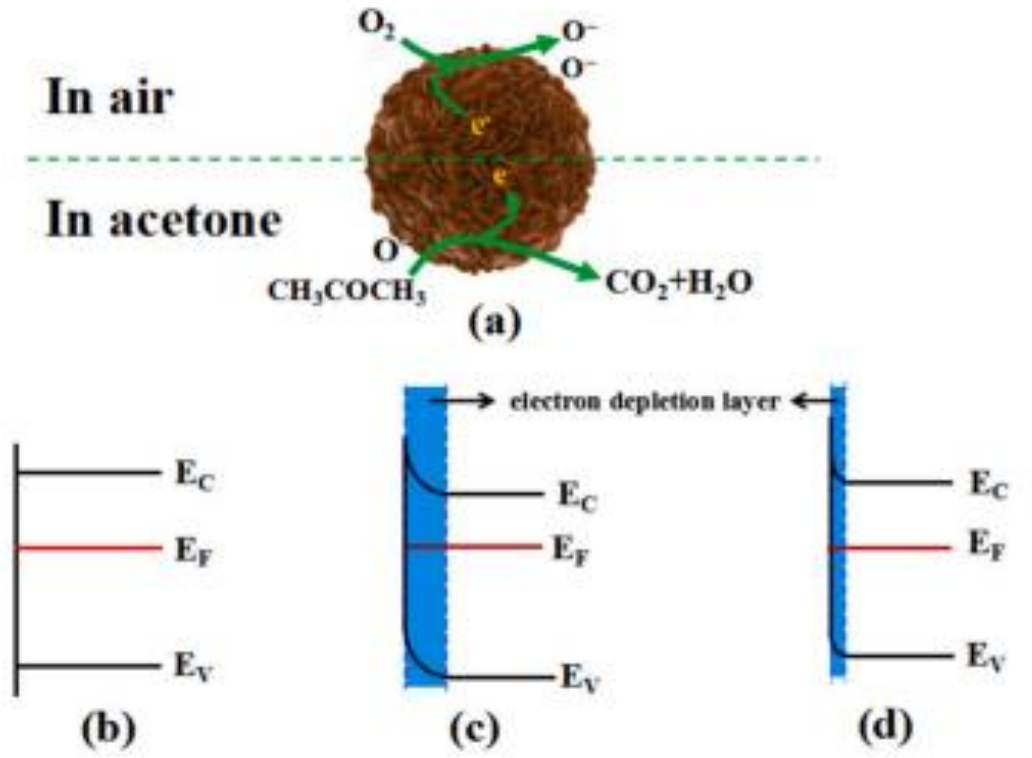

Figure 2.7: (a) The α-Fe_2O_3 sensor's gas detection algorithm is illustrated in the diagram above. Diagrams of surface state band diagrams in various environments :(b) without air; (c) in the atmosphere (d) when there is acetone present [**34]**

Reference

1. Abid, N., et al., *Synthesis of nanomaterials using various top-down and bottom-up approaches, influencing factors, advantages, and disadvantages: A review.* Advances in Colloid and Interface Science, 2021: p. 102597.
2. Hjiri, M., et al., *Al-doped ZnO for highly sensitive CO gas sensors.* Sensors and Actuators B: Chemical, 2014. **196**: p. 413-420.
3. Arshak, K., et al., *A review of gas sensors employed in electronic nose applications.* Sensor review, 2004.
4. Chiu, H.-C. and C.-S. Yeh, *Hydrothermal synthesis of SnO_2 nanoparticles and their gas-sensing of alcohol.* The Journal of Physical Chemistry C, 2007. **111**(20): p. 7256-7259.
5. Carotta, M., et al., *ZnO gas sensors: a comparison between nanoparticles and nanotetrapods-based thick films.* Sensors and Actuators B: Chemical, 2009. **137**(1): p. 164-169.
6. Giberti, A., et al., *Permittivity measurements in nanostructured TiO_2 gas sensors.* physica status solidi (a), 2011. **208**(1): p. 118-122.
7. Urasinska-Wojcik, B., et al., *Ultrasensitive WO_3 gas sensors for NO_2 detection in air and low oxygen environment.* Sensors and Actuators B: Chemical, 2017. **239**: p. 1051-1059.
8. Mirzaei, A., B. Hashemi, and K. Janghorban, *α-Fe_2O_3 based nanomaterials as gas sensors.* Journal of Materials Science: Materials in Electronics, 2016. **27**(4): p. 3109-3144.
9. Volanti, D.P., et al., *The role of hierarchical morphologies in the superior gas sensing performance of cuo-based chemiresistors.* Advanced Functional Materials, 2013. **23**(14): p. 1759-1766.
10 Yu, Y., et al., *Synthesis of multiple networked NiO nanostructures for enhanced gas sensing performance.* Materials Letters, 2017. **206**: p. 80-83.
11. Pokhrel, S., et al., *Investigations of conduction mechanism in Cr_2O_3 gas sensing thick films by ac impedance spectroscopy and work function changes measurements.* Sensors and Actuators B: Chemical, 2008. **133**(1): p. 78-83.

12. Nikolic, M.V., et al., *Structural, morphological and textural properties of iron manganite ($FeMnO_3$) thick films applied for humidity sensing.* Materials Science and Engineering: B, 2020. **257**: p. 114547.
13. Tripathy, A., et al., *Design and development for capacitive humidity sensor applications of lead-free Ca, Mg, Fe, Ti-oxides-based electro-ceramics with improved sensing properties via physisorption.* Sensors, 2016. **16**(7): p. 1135.
14. Tulliani, J.-M., et al., *Strontium-doped hematite as a possible humidity sensing material for soil water content determination.* Sensors, 2013. **13**(9): p. 12070-12092.
15. Falsafi, F., et al., *Sm-doped cobalt ferrite nanoparticles: A novel sensing material for conductometric hydrogen leak sensor.* Ceramics International, 2017. **43**(1): p. 1029-1037.
16. Shankar, P. and J.B.B. Rayappan, *Gas sensing mechanism of metal oxides: The role of ambient atmosphere, type of semiconductor and gases-A review.* Sci. Lett. J, 2015. **4**(4): p. 126.
17. Senthilkumar, P., et al., *Antibacterial activity of neem extract and its green synthesized silver nanoparticles against Pseudomonas aeruginosa.* Journal of Pure and Applied Microbiology, 2018. **12**(2): p. 969-974.
18. Samrot, A.V., N. Shobana, and R. Jenna, *Antibacterial and antioxidant activity of different staged ripened fruit of Capsicum annuum and its green synthesized silver nanoparticles.* BioNanoScience, 2018. **8**(2): p. 632-646.
19. Patil, R.M., et al., *Comprehensive cytotoxicity studies of superparamagnetic iron oxide nanoparticles.* Biochemistry and biophysics reports, 2018. **13**: p. 63-72.
20. Pallela, P.N.V.K., et al., *Antibacterial efficacy of green synthesized α-Fe_2O_3 nanoparticles using Sida cordifolia plant extract.* Heliyon, 2019. **5**(11): p. e02765.
21. Mohapatra, M. and S. Anand, *Synthesis and applications of nano-structured iron oxides/hydroxides–a review.* International Journal of Engineering, Science and Technology, 2010. **2**(8).
22. Lassoued, A., et al., *Control of the shape and size of iron oxide (α-Fe_2O_3) nanoparticles synthesized through the chemical precipitation method.* Results in physics, 2017. **7**: p. 3007-3015.
23. Modan, E.M., et al., *NANOSTRUCTURED IRON OXIDE POWDERS BY MICROWAVE ASSISTED SYNTHESIS.* Journal of Science and Arts, 2021. **21**(4): p. 1081-1094.

24.Devi, S., et al., *Phase transformation and structural evolution in iron oxide nanostructures.* Materials Science and Engineering: B, 2021. **272**: p. 115329.
25.Kumar, P., et al., *Investigations on magnetic and electrical properties of Zn doped Fe_2O_3 nanoparticles and their correlation with local electronic structures.* Journal of Magnetism and Magnetic Materials, 2019. **489**: p. 165398.
26.Jabbar, K.Q., A.A. Barzinjy, and S.M. Hamad, *Iron oxide nanoparticles: Preparation methods, functions, adsorption and coagulation/flocculation in wastewater treatment.* Environmental Nanotechnology, Monitoring & Management, 2022. **17**: p. 100661.
27.Hoa, N.D., et al., *General and scalable route to synthesize nanowire-structured semiconducting metal oxides for gas-sensor applications.* Journal of alloys and compounds, 2013. **549**: p. 260-268.
28.Jagadeesh, R.V., et al., *Nanoscale Fe_2O_3-based catalysts for selective hydrogenation of nitroarenes to anilines.* Science, 2013. **342**(6162): p. 1073-1076.
29.Hung, C.M., et al., *Synthesis and gas-sensing characteristics of α-Fe_2O_3 hollow balls.* Journal of Science: Advanced Materials and Devices, 2016. **1**(1): p. 45-50.
30.Kim, D.H., et al., *Vertically ordered hematite nanotube array as an ultrasensitive and rapid response acetone sensor.* ACS Applied Materials & Interfaces, 2014. **6**(17): p. 14779-14784.
31.Shah, V., et al., *Room-Temperature Chemiresistive Gas Sensing of SnO_2 Nanowires: A Review.* Journal of Inorganic and Organometallic Polymers and Materials, 2022: p. 1-32.
32.Gautam, Y.K., et al., *Nanostructured metal oxide semiconductor-based sensors for greenhouse gas detection: Progress and challenges.* Royal Society open science, 2021. **8**(3): p. 201324.
33.Garcia, D., et al., *Sensors based on Ag-loaded hematite (α-Fe_2O_3) nanoparticles for methyl mercaptan detection at room temperature.* Analytical chemistry research, 2017. **12**: p. 74-81.
34.Qin, Q., X. Zhu, and X. Zhang, *Synthesis of α-Fe_2O_3 hollow spheres with rapid response and excellent selectivity towa rds acetone.* Materials Science and Engineering: B, 2022. **275**: p. 115482.

Chapter 3

3 Synthesis and characterisation of alpha iron oxide

3.1 Sample preparations

In this study, the chemical precipitation method was identified as the desired route to prepare the samples of pure alpha iron oxide (α-Fe_2O_3) and ruthenium doped samples due to the following reasons: low cost, short preparation time for the formation of samples, high homogeneity, and a highly crystalline, and generally low reaction temperature. Iron (Ⅲ) chloride hexahydrate ($FeCl_3.6H_2O$) was the precursor while the ammonia solution (NH_4OH) was the precipitating agent. The sample was washed with ethanol, and all the solutions were prepared with distilled water **[1]**. The samples of pure α-Fe_2O_3 and ruthenium doped were obtained by using the method summarised in Fig. 3.1.

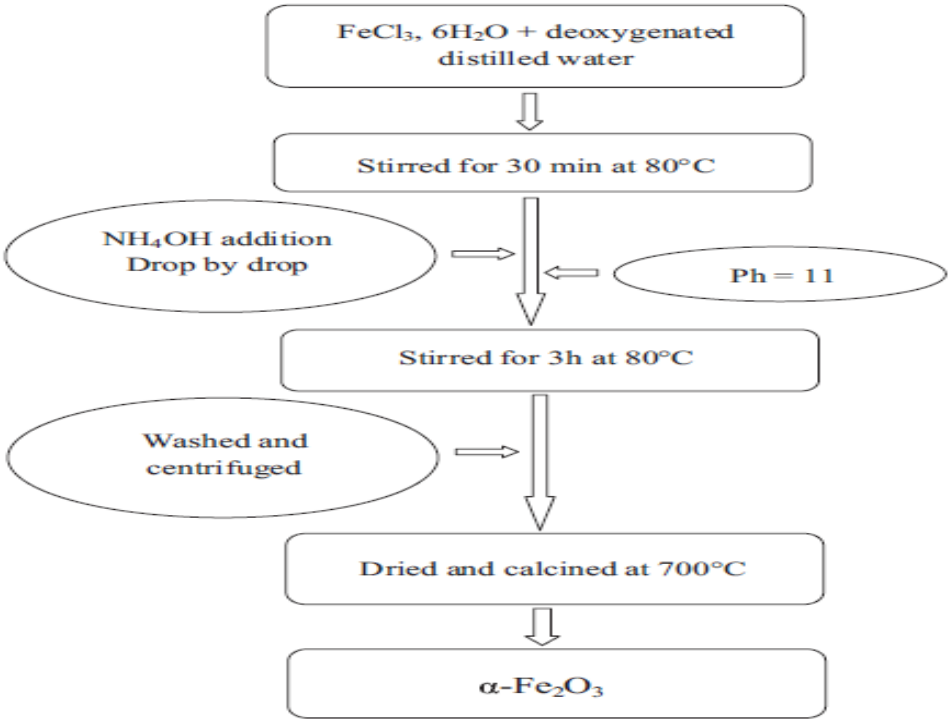

Figure 3.1: Flow chart for the synthesis of hematite of alpha-iron oxide nanoparticles **[1].** A brief description of the process follows:

In a beaker, 100ml of deoxygenated distilled water was mixed well with a mass of Iron (III) chloride hexahydrate ($FeCl_3.6H_2O$). A magnetic stirrer was used to stir the solution for 30 minutes while the temperature was fixed at 80ºC to obtain 0.1 M which is the concentration of the solution. To determine the effect of concentration on the size of the material, a similar method was used to obtain 0.08 M, 0.07 M, 0.06 M, 0.05 M, and 0,03M solutions. Ammonia hydroxide (NH_4OH) was used as a precipitating agent, adding drops of it gradually to maintain pH 11. Under magnetic stirring, the solution was heated for 3 hours. The precipitated product was collected by centrifugation (6000rpm) machine. The product was washed several times with ethanol and distilled water. After the product had been dried for 3 hours at 80° C in an oven it was calcined in the open air for 4 hours at 700° C to form a material with sharper, stronger peaks of alpha iron oxide undoped and doped samples **[**1]. **Eq. 3.1** and **3.2** explain how the final product of the samples of alpha iron oxide and ruthenium doped samples were obtained.

$$FeCl_3 + H_2O + NH_4OH \longrightarrow FeOOH + 2HCl + NH_4Cl, \quad (3.1)$$

$$FeOOH \xrightarrow{\Delta} 700ºC \ \alpha\text{-}Fe_2O_3, \quad (3.2)$$

The colour of the final product for all doped samples was found to be black while the pure alpha iron oxide was dark red (**see Fig. 3.2 a-b**).

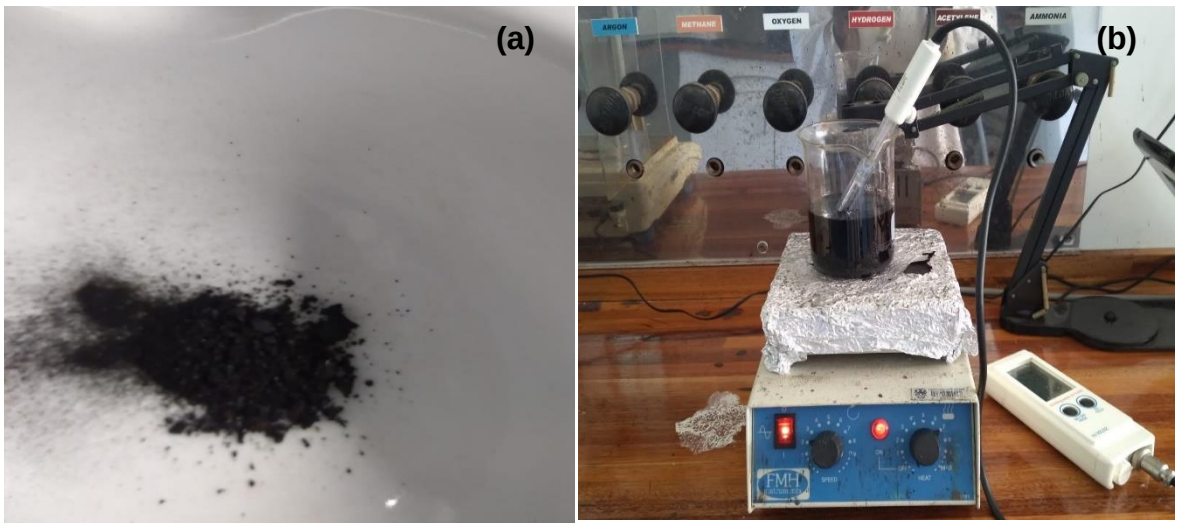

Figure 3.2: Preparation of the sample of α-Fe_2O_3-Ru under the magnetic stirring bar. A pH meter was used to control the pH of the solution (Pictures taken in the UNIZULU Lab).

3.2 Synthesis of hematite (α- Fe_2O_3)

Different synthesis techniques for hematite particles have been developed such as hydrothermal techniques, sol-gel techniques, and the poly method **[2]**,**[3],** and the chemical method **[1]**. In this study, the chemical precipitation method was used to synthesise alpha iron oxide**.** The shape and size of the particles depend on the synthesis parameters, including the reactant concentration, reaction temperature, and pH levels of the solution.

3.3 Characterisation techniques

3.3.1 Characterisation of alpha iron oxide

The samples were subjected to different characterisation techniques. These techniques were X-ray diffraction (XRD), scanning electron microscopy (SEM), high resolution-transmission electron microscopy (HR-TEM), X-ray Photoelectron Spectroscopy (XPS), Thermogravimetric analysis (TGA), Brunauer-Emmett-Teller (BET), and this chapter gives a brief overview of how they were utilised.

3.3.2 X-Ray Diffraction (XRD)

X-ray diffraction is a powerful instrument used in the research industry. It was created by W.C. Rontgen in the year 1895 **[4]**. An X-ray tube can be used to generate X-rays in a laboratory by heating the filament and accelerating electrons towards a target, as shown in **Fig 3.3**.

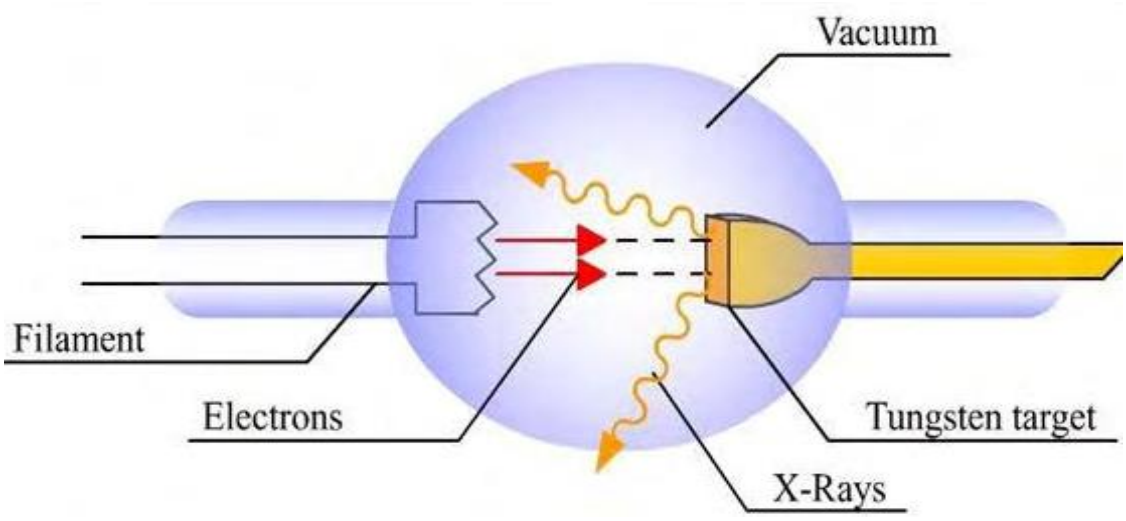

Figure 3.3: The process of producing X-rays in the laboratory **[4].**

When the target collides with the beam, X-rays are generated. In X-ray spectra, characteristic X-ray spectra are produced (see **Fig 3.3**) when electrons possess enough energy to dislodge electrons from the target material's inner shell.

An X-ray source of Cu Kα radiations with a wavelength of (ʎ = 1.5418 Å), was used to determine the unknown crystalline compounds. The diffraction parameter such as scan steps, collection time, range, and the current-voltage were fixed based on the specimens requirement analysis **[5]**.The crystal size and growth of a particular material can also be determined through X-ray diffraction, as well as the symmetry of the unit cell. The atoms have been arranged in the periodic lattices with the (d-spacing). The interaction of incident X-rays with a single crystal produces constructive interference from the parallel plane if the condition of Bragg's law is satisfied see **Fig.3.4 [6].**

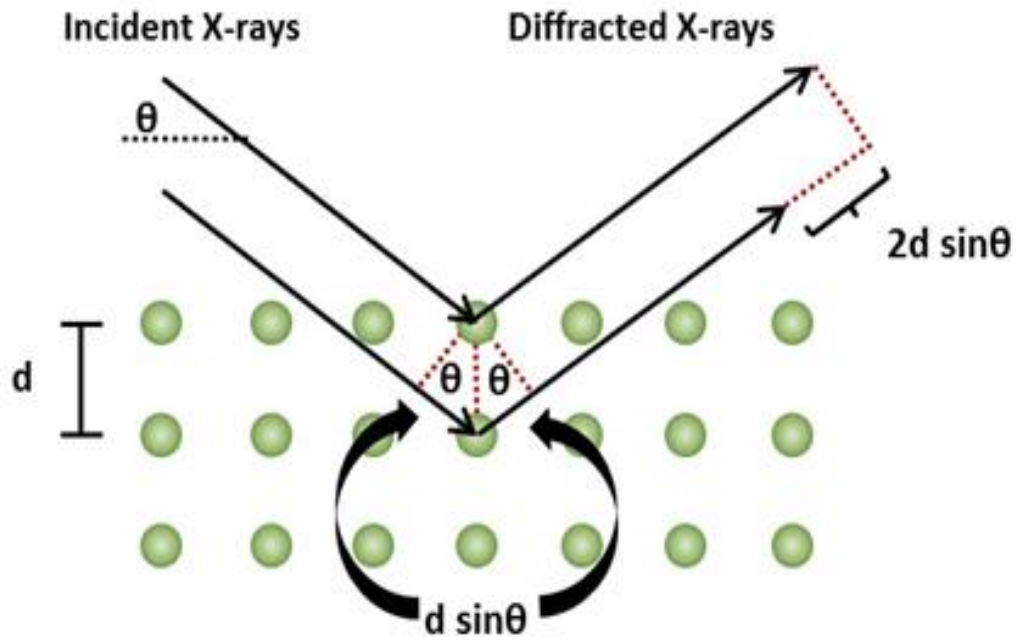

Figure 3.4: The Bragg's law conditions **[6].**

The above figure can be also explained in terms of Bragg's law in **Eq. 3.3**, which states that if an X-ray is an incident into a crystal surface at a normal angle of incident θ, it would reflect with the same scattering angles, and if the path difference indicated by d is equal to any whole number n, of the wavelength λ, constrictive interference is simply possible.

$$n\lambda = 2dsin\theta, \qquad (3.3)$$

The crystallographic plane is very useful in crystal to determine the direction and distance and are identified by Miller indices (*hkl)* for the cubic crystal with a lattice parameter, *a* The interplanar corresponding to the specific (*hkl)* is given by the equation.

$$D_{hkl} = \frac{a}{\sqrt{h^2+k^2+l^2}} \qquad (3.4)$$

The **Debye-Scherer equation** is the major formula that can relate the size of the particles in the solid to the broadening of specific peaks that are present in the diffraction pattern in both X-ray diffraction and crystallography. It is mostly used to calculate particle sizes under 60 nm. It is given in **Eq.3.5**

$$D = \frac{k\lambda}{\beta cos\theta_B} \qquad (3.5)$$

where D is the particles size, k is the dimensionless shape factor and usually has the value of 0.9, λ is the x-ray wavelength (in nm), β_{hkl} is the full-width-half-maximum (FWHM) value of the diffraction signal (in radians), and β on $cos\theta_B$ is the angle at which the peak of the signal occurs **[6]**. In this project, XRD was used for the structural analysis of the compounds produced. The measurements were done in the department of Chemistry (UNIZULU) by using the D8 advanced XRD diffractometer as shown in **Fig. 3.5** below. This D8 Advanced XRD works in the following way. A small portion of fine powder samples (alpha iron oxide and ruthenium doped samples) was placed on the sample holder. The sample holder together with the sample was placed in the system D8 diffractometer. The x-ray diffraction pattern of the samples was determined using a German Bruker D8 PHASER x-ray diffraction system with Cu/K as the radiation source with the wavelength of λ = 1.5418 Å), and data were collected in the range of 10 to 80 degrees at a scanning speed of 0.5, which is equivalent to 45 minutes per sample. Then the machine was stopped, and data was taken from the on-screen monitor at the lab.

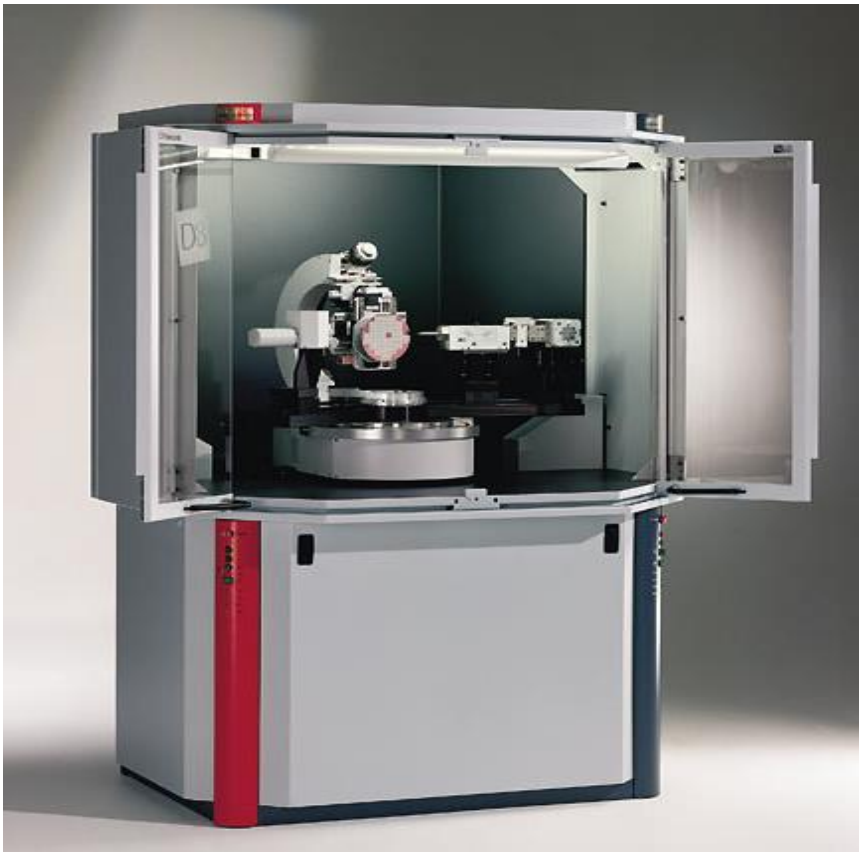

Figure 3.5: D8 Advanced for XRD measurement

3.3.3 Scanning electron microscopy (SEM)

Scanning electron microscopes (SEMs) are used to analyse the surface morphology of materials, and topology **[7]**. Electron beams are accelerated by electrostatic or electromagnetic lenses to create images of high resolution based on the short wavelengths of the electrons as compared to visible light photons. The approach also provides information on crystalline structure, chemical compositions, and element mapping. Depending on the properties and type of the sample, the electron interacts with the sample from a few nanometres to the micrometres range, and this causes backscattering and the emission of a second electron as show in **Fig. 3.6.**

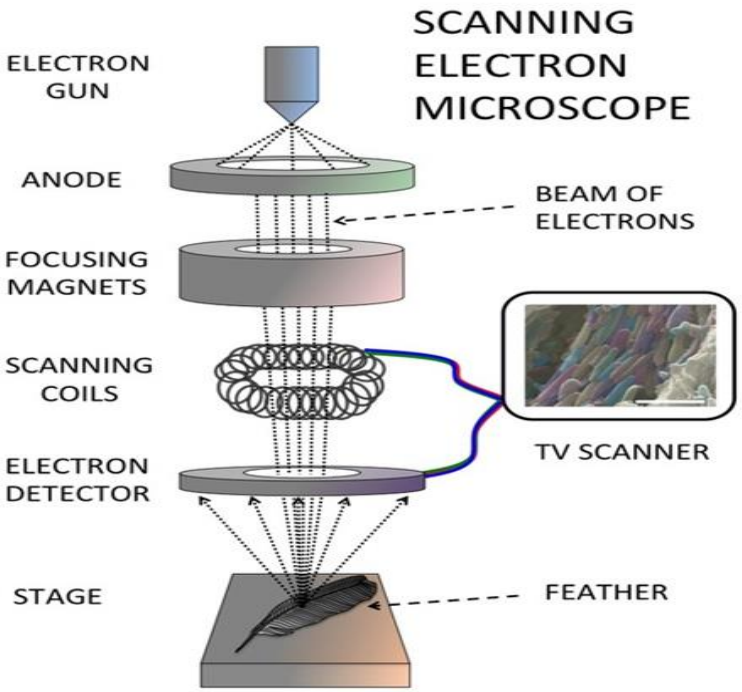

Figure 3.6: Schematic diagram representing the basic components of scanning electron microscopy (SEM) **[7].**

Scanning electron microscopy (SEM) is described in the steps below:

- An image is displayed on the screen.
- With larger magnifications it provides a two-dimensional image of the surface of the sample.
- A large depth of field allows more of the spacimen to be focused on.
- The sample is placed on the lower level of the chamber.

Different modes of scanning electron microscopy (SEM) exist for the characterisation of the material (including Biomaterial) such as X-ray mapping, Second electron imaging, Back Scatted electron imaging, and electron channeling **[8]**. One of the reasons why SEM is preferred for particle size analysis is that it has a resolution of 10nm (100 Å), and an advanced version of this instrument can achieve a resolution of 2.5 nm (25 Å). The structure or orientations of small crystals or features can be determined using EDX, EDS, EDAX, or similar procedures and techniques. The advantage of SEM is that it provides detailed information via three-dimensional (3D) images and versatile information. However, this technique is very expensive and only

applicable to solid, inorganic samples small enough to fit within a vacuum chamber capable of handling moderate vacuum pressure **[8, 9]**.

3.3.4 HR-TEM (High-Resolution Transmission Electron Microscopy)

An electrical engineer from Germany named Max Knoll and Ruska created a device he called the high-resolution transmission electron microscopy (TEM) in 1931. TEM uses the same principle as SEM, using electrons as an excitation source, but uses high acceleration voltages (100-300kV) to achieve a sharp image, typically in the range of (0.1-0.2) nm. Some features with characteristic dimensions below 100 nm (and even atomic scales) may be studied with TEMs in the fields of biology, materials science, and engineering. The analysis provides information on the morphology, shape, and size of the sample, chemical composition, and even chemical bonding characteristics **[4, 10-12]**. (**Fig.3.7 a-b**) shows the Schematic diagram and a photograph of a transmission electron microscope.

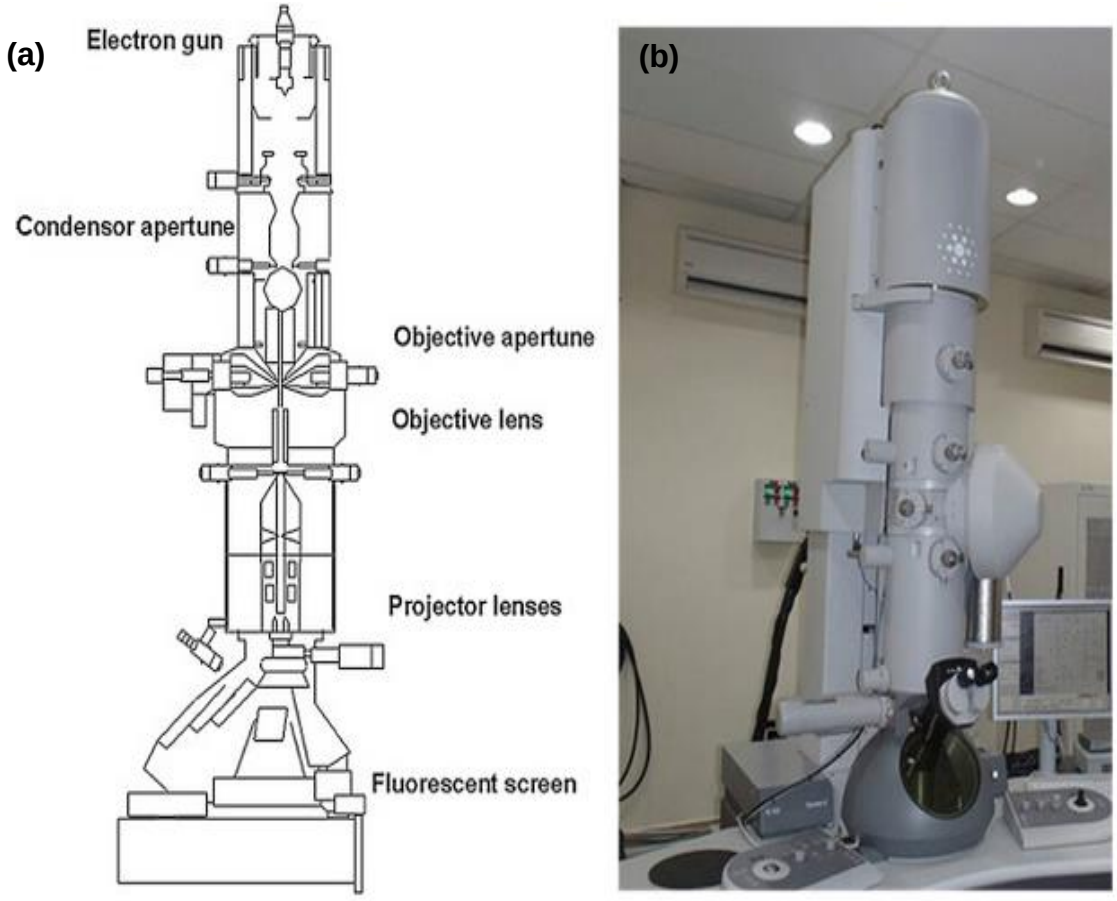

Figure 3.7: Schematic diagram (a), and (b) a photograph of a transmission electron microscope **[4].**

3.3.5 X-ray Photoelectron Spectroscopy (XPS)

By using the bundling energy of photoelectron emission, except for hydrogen and helium, XPS can identify all solid and liquid elements. XSP is a method that detects photoelectron emission from a sample after it has been irradiated with a single-energy X-ray photon. In addition, this technique provides information on the composition of the element, the chemical formula as well as the empirical formula, and also the electrical state of the element, including the material. **Fig 3.8** shows the schematic representation of an X-ray Photoelectron Spectroscope **[13-16]**.

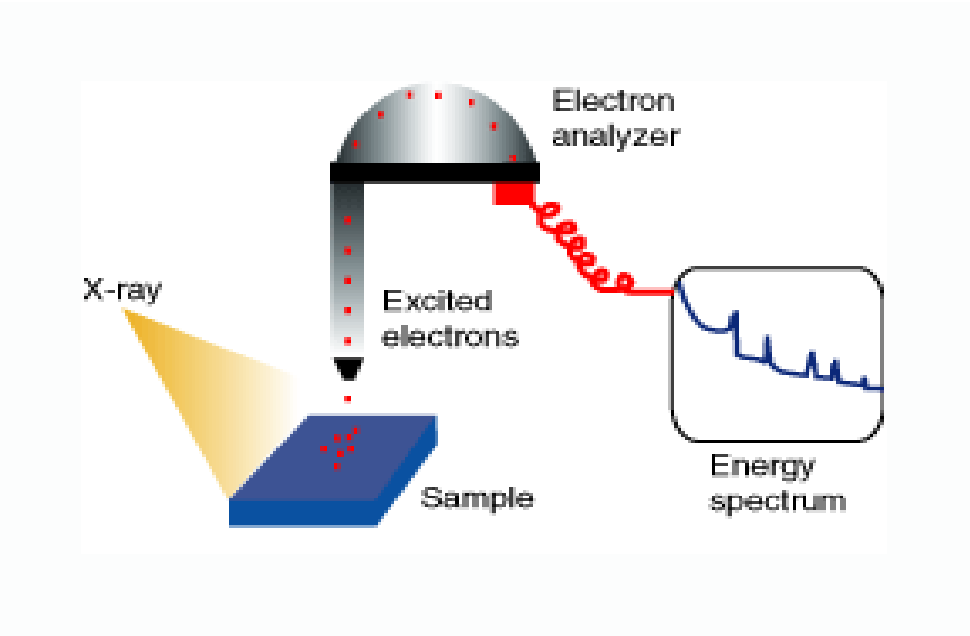

Figure 3.8: Schematic representation of an X-ray Photoelectron Spectroscope **[16].**

3.3.6 Brunauer-Emmett-Teller (BET)

An important purpose of this technique is to determine how gas molecules adhere to the surface of a solid and serve as the basis for important analytical techniques for analysing specific areas of the material. This method of BET is typically used to determine the specific surface area (SSA) of nitrogen adsorption isotherms at 77.0 K, with pressure ranges of 0.05 to 0.3 P/P_0 relative to the temperature. Adsorption is the process by which gas atoms or molecules are attached to a surface. Moreover, a certain quantity of gas being adsorbed depends on the total area of the material exposed to the gas. The temperature, and pressure of a gas, as well as the quality of

interaction which is in between the gas molecular, and the strong interaction between the gas molecular and the sold molecular. Analysing surfaces by using the BET since it is available, and it consists of high purity and interacts strongly with most solids by using Nitrogen. The interaction between the gas and the solid phase is usually weak, so anything cooled using N_2 to obtain a detectable adsorption level and a known amount of nitrogen gas is gradually released into the sample cell. In creating a partial vacuum condition, a relative pressure that is below atmospheric pressure is achieved **[16]**.

3.3.7 Thermogravimetric Analysis (TGA)

Thermogravimetric Analysis is one of the most powerful methods for determining a material's thermodynamic stability. In general, the test for TGA is done as the function of the temperature rise at a constant rate or as the function of the mass and temperature over time. The change in the mass of the samples is measured by using a highly sensitive balance**[17]**. The instrument consists of an electronic balance and a control microprocessor, which communicates with the process station data when it is inside an oven. Powder samples are placed in the analysis equipment to be tested, then calcined to 1000º C per minute as shown in **Fig 3.9**.

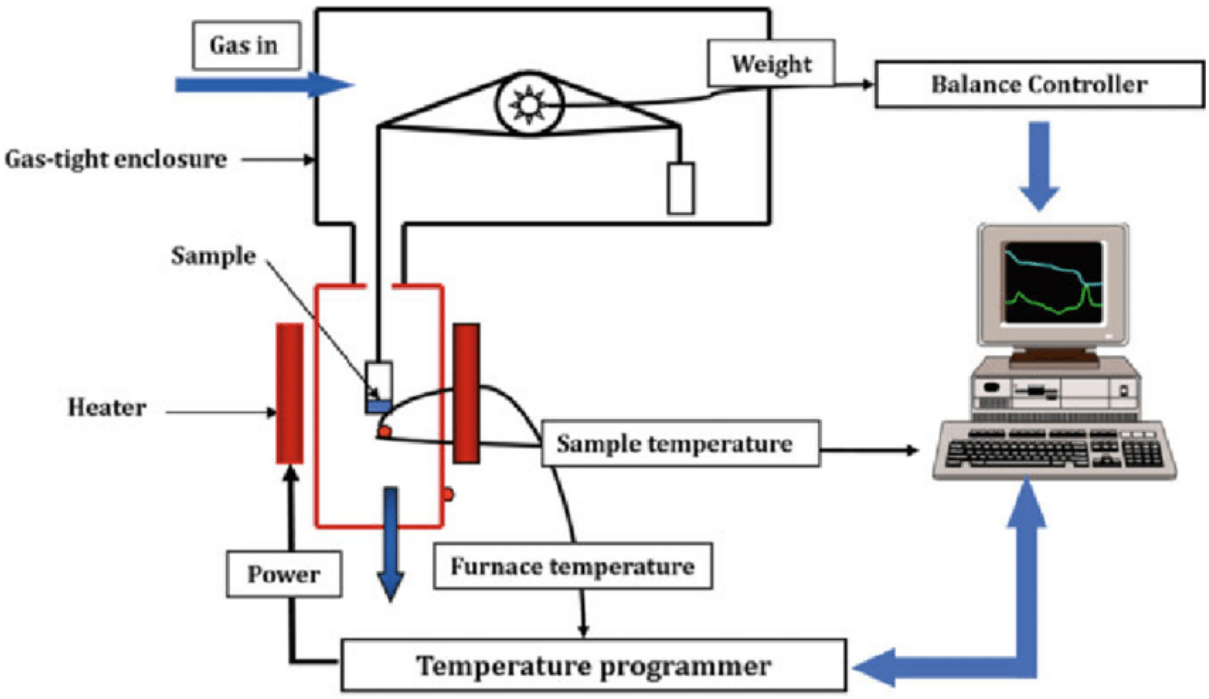

Figure 3.9: schematic diagram of TGA setup **[17].**

3.4 Gas sensing

3.4.1 Gas sensing properties alpha iron oxide (α-Fe_2O_3)

Gas sensors are an important family of electronic devices widely used in industrial and home applications. The basic principle of this type of sensor is based on the reaction of gas molecular and semiconductor surfaces **[18]**. Metal oxide semiconductor (MOS) gas sensor operates on the principle of chemo resistance by changing the electrical conductivity or resistivity of a thin film when exposed to a target gas. This interaction between the gas molecule and the device typically acts as a donor or acceptor for charge carriers, altering the resistivity of the metal oxide. The nature of the reaction is determined by the nature of the charge carriers in the semiconductor film and the nature of the molecules of the exposed gas (oxidising or reducing gas). Gas sensor performance depends on sensitivity, selectivity, stability, response, and recovery time. The time required to reach 90% of the saturation level is called the response, and recovery time is the time required to reach 10% of the saturation level when exposed to a clean environment **[19, 20]**. In the study, alpha iron oxide and ruthenium doped were expected to improve the sensitivity of the material. We also know that alpha iron oxide alone can be used as the sensing material since it has good properties for gas sensing towards different gas. **Fig. 3.11** shows an example of alpha iron oxide response towards carbon monoxide gas. **Fig. 3.10(a)** shows the example to further explain the concept of how the material behaves when it is exposed to the target gas; in this case it was for alpha iron pure. **Fig. 3.10 (b)** shows the responses of alpha iron oxide doped with the other material, while **Fig. 3.10 (c)** shows the response of pure alpha and doped samples. This simply means that it is possible to increase the response of the material by doping it with other material. **Fig. 3.10(d)** shows the increase in the response if the dopant concentration is increased. This means that alpha iron doped with rGo is more selective to CO gas if the concentration is 0.03.

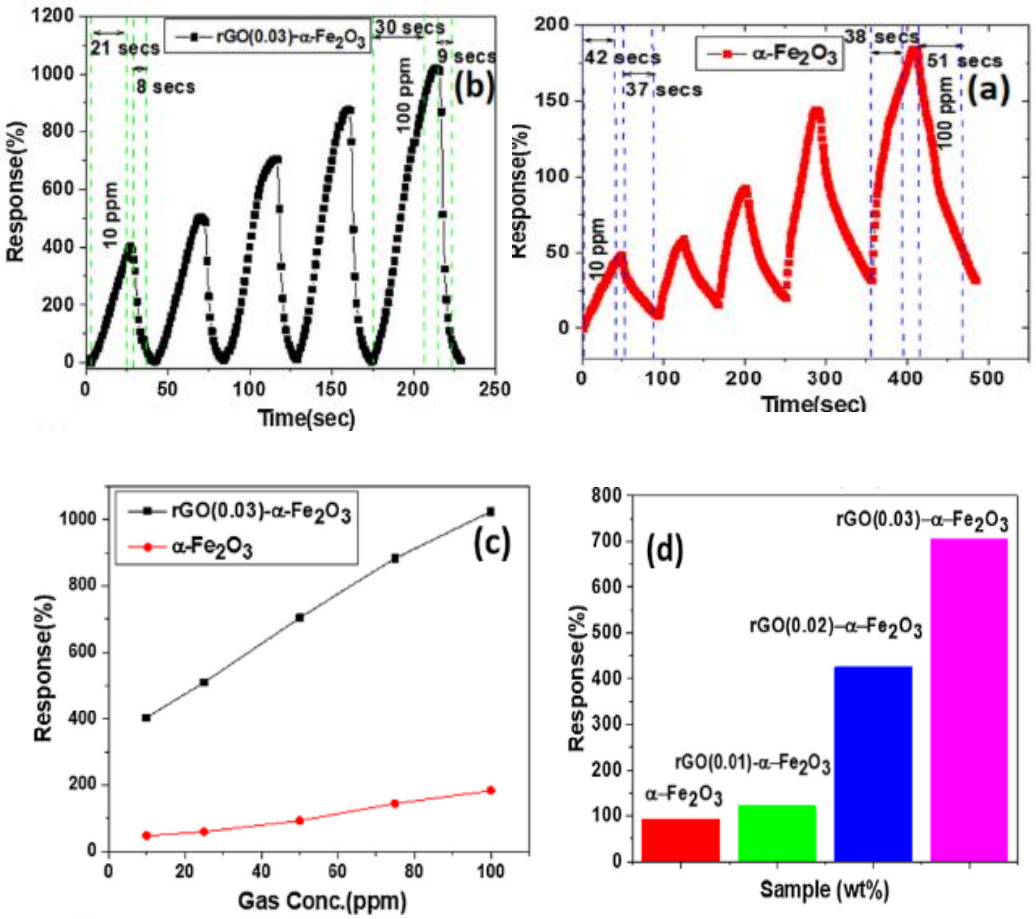

Figure 3.10 : (a) α-Fe_2O_3 – response towards a different level of CO gas (b) Experimental results of rGO(0.03)-α-Fe_2O_3 composites at different levels of CO gas ppm (c) rGO(0.03)-α-Fe_2O_3 and α-Fe_2O_3 at varying levels of ppm (d) Experimental response to α-Fe_2O_3, rGO(0.01, 0.02, 0.03)-α-Fe_2O_3 operated at 50 ppm CO gas at room temperature **[21, 22]**.

Sensor sensitivity is defined as the ratio of resistance in the air to resistance after exposure to the analysed gas. The sensitivity of gas sensors depends on the types of semiconductors since we have n-type semiconductors and p-type semiconductors. The calculation of sensitivity for n-type semiconductors is given by **equation 3.6**:

$$S = \frac{Rair}{Rgas} \qquad (3.6)$$

while that for sensitivity for p-type semiconductors is given by equation 3.7:

$$S = \frac{Rgas}{Rair} \qquad (3.7)$$

The percentage for n-type semiconductors is calculated by equation 3.8.

$$\mathbf{S\ (\%) = \left(\frac{R_{air}-R_{gas}}{R_{air}}\right) \times 100}, \qquad (3.8)$$

where, R_{air} is the resistance of the gas sensor before it passes the gas and R_{gas} is the resistance after passing the gas and reaching the saturation values.

3.3.2 Fabrication of the gas sensor measurements

The chemical precipitation method was used to obtain the samples, and to fabricate the sensor. The following steps explain how the sensor was made:

- Small samples were placed on the test vial.
- Ethanol was added to the test vial, and the solution was shaken until completely mixed.
- An ultrasonic bath was used to sonicate the mixture for approximately one hour.
- Drop-cast mixture was placed on alumina substrates that were pre-printed with electrodes on one side. An example of the substates being used is given in **Fig.3.11.**
- To remove the residue of ethanol from the thin sensor layer, it was dried at a temperature of 120 °C.
- Finally, those sensors were tested for gas sensing performance by using the KENOSISTEC machine shown on the **Fig.3.12.**

α-Fe_2O_3 and Ru-doped were tested over flammable and hazardous gases i.e., liquefied petroleum gases (LPGs), ammonia (NH_3), hydrogen sulfide (H_2S), and hydrogen (H_2). The operating temperature of the fabricated sensor was also investigated to find the optimum temperate. In addition, the best performing (MOS) was then subjected to repeatable and stability measurements to test the quality of the sensor over time. The structure of the gas sensor of NO_2 shown in **Fig.3.11** is used as an example to show what alumina substrates used in this study looked like. It is pre-printed with electrodes on one side and also consists of the wire that we used to corneting the ohmic contact from the complete circuit.

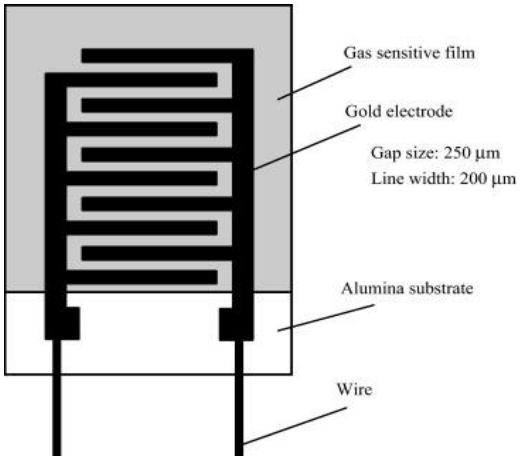

Figure 3.11: Structure of NO_2 gas sensor **[23]**

Figure 3.12: A KENOSISTEC Gas Sensor Tester of the Physics Department, University of Zululand.

Figure 3.13: The climatic test chamber of the KENOSISTEC instrument.

The sensor was placed inside the chamber shown in the **Fig 3.13** above. It was made from stainless steel to allow for the rapid changes in the process, and the chamber volume was set to less than 500 ccs. KENOSISTEC gas-sensing machines have been used in several studies to investigate the gas-sensing properties of different gas sensors **[24]**.

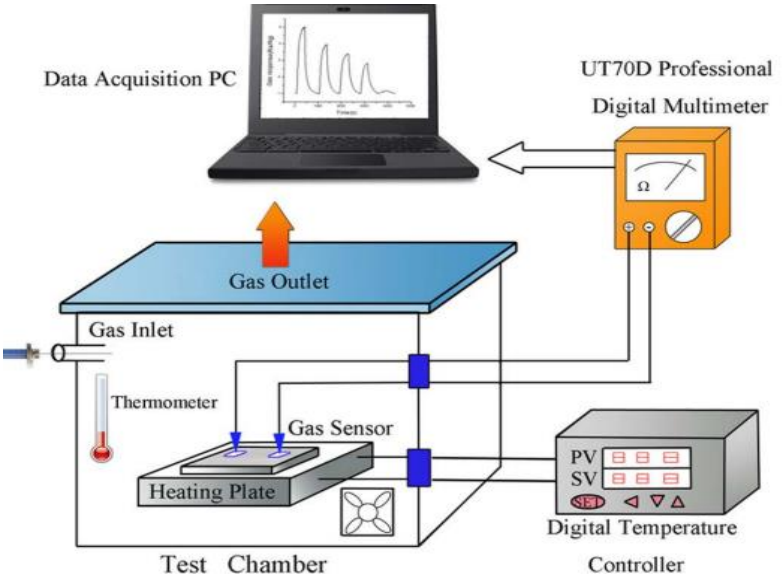

Figure 3.14: shows the schematic of gas being introduced into the system **[24].**

A digital MultiMate (**Fig.3.14**) is used to measure changes in the resistance of the material being used at a specific time, and data is obtained via a data acquisition system.

Reference

1. Lassoued, A., et al., *Control of the shape and size of iron oxide (α-Fe2O3) nanoparticles synthesized through the chemical precipitation method.* Results in physics, 2017. **7**: p. 3007-3015.
2. Hassan, H.S., et al., *Fabrication and characterization of gas sensor micro-arrays.* Sensing and Bio-Sensing Research, 2014. **1**: p. 34-40.
3. Bandgar, D., et al., *Novel route for fabrication of nanostructured α-Fe2O3 gas sensor.* Materials science in semiconductor processing, 2014. **17**: p. 67-73.
4. Mokoena, T.P., *Synthesis and luminescent properties of aluminium oxide-titanium dioxide nanocomposites doped with different rare-earths ions*. 2016, University of the Free State.
5. Daou, I., et al., *Probing the dehydroxylation of kaolinite and halloysite by in situ high temperature x-ray diffraction.* Minerals, 2020. **10**(5): p. 480.
6. Fouad, D.E., et al., *Improved size, morphology and crystallinity of hematite (α-Fe2O3) nanoparticles synthesized via the precipitation route using ferric sulfate precursor.* Results in Physics, 2019. **12**: p. 1253-1261.
7. Van Hoang, N., et al., *Excellent detection of H2S gas at ppb concentrations using ZnFe2O4 nanofibers loaded with reduced graphene oxide.* Sensors and Actuators B: Chemical, 2019. **282**: p. 876-884.
8. Brodusch, N., et al., *Scanning Electron Microscopy versus Transmission Electron Microscopy for Material Characterization: A Comparative Study on High-Strength Steels.* Scanning, 2021. **2021**.
9. Webb, R.I. and N.L. Schieber, *Volume scanning electron microscopy: serial block-face scanning electron microscopy focussed ion beam scanning electron microscopy*, in *Cellular Imaging*. 2018, Springer. p. 117-148.
10. Tang, C. and Z. Yang, *Transmission electron microscopy (TEM)*, in *Membrane characterization*. 2017, Elsevier. p. 145-159.
11. Abbasi, Y.F. and H. Bera, *Konjac glucomannan-based nanomaterials in drug delivery and biomedical applications*, in *Biopolymer-Based Nanomaterials in Drug Delivery and Biomedical Applications*. 2021, Elsevier. p. 119-141.
12. Murugesan, B., et al., *Fabrication of palladium nanoparticles anchored polypyrrole functionalized reduced graphene oxide nanocomposite for*

antibiofilm associated orthopedic tissue engineering. Applied Surface Science, 2020. **510**: p. 145403.

13. Baer, D.R. and S. Thevuthasan, *Characterization of thin films and coatings*, in *Handbook of Deposition Technologies for Films and Coatings*. 2010, Elsevier. p. 749-864.
14. Addepalli, S., *Industrial applications of X-Ray Photoelectron Spectroscopy (XPS) in India.* Journal of Electron Spectroscopy and Related Phenomena, 2019. **231**: p. 11-42.
15. Stevie, F.A., et al., *Sample handling, preparation and mounting for XPS and other surface analytical techniques.* Journal of Vacuum Science & Technology A: Vacuum, Surfaces, and Films, 2020. **38**(6): p. 063202.
16. Kloprogge, J.T., C.P. Ponce, and T. Loomis, *The Periodic Table: Nature's Building Blocks: An Introduction to the Naturally Occurring Elements, Their Origins and Their Uses*. 2020: Elsevier.
17. Zafeiropoulos, N.E., *Interface engineering of natural fibre composites for maximum performance*. 2011: Elsevier.
18. Saleem, H., et al., *Advances of nanomaterials for air pollution remediation and their impacts on the environment.* Chemosphere, 2022. **287**: p. 132083.
19. Hjiri, M., et al., *Al-doped ZnO for highly sensitive CO gas sensors.* Sensors and Actuators B: Chemical, 2014. **196**: p. 413-420.
20. Navale, S., et al., *Synthesis of Fe2O3 nanoparticles for nitrogen dioxide gas sensing applications.* Ceramics International, 2013. **39**(6): p. 6453-6460.
21. Basu, A.K., et al., *α-Fe2O3 loaded rGO nanosheets based fast response/recovery CO gas sensor at room temperature.* Applied Surface Science, 2019. **465**: p. 56-66.
22. Li, Z., et al., *A fast response & recovery H2S gas sensor based on α-Fe2O3 nanoparticles with ppb level detection limit.* Journal of hazardous materials, 2015. **300**: p. 167-174.
23. Su, P.-G. and T.-T. Pan, *Fabrication of a room-temperature NO2 gas sensor based on WO3 films and WO3/MWCNT nanocomposite films by combining polyol process with metal organic decomposition method.* Materials Chemistry and Physics, 2011. **125**(3): p. 351-357.

24. Van Hieu, N., et al., *Gas-sensing properties of tin oxide doped with metal oxides and carbon nanotubes: A competitive sensor for ethanol and liquid petroleum gas.* Sensors and Actuators B: Chemical, 2010. **144**(2): p. 450-456.

Chapter 4

4 Results and discussion

This chapter presents the results of hematite dope with different weight percentages of ruthenium. The samples were prepared by chemical precipitation methods and drop-casting methods were used to fabricate the sensors. The samples were characterised by X-ray diffraction (XRD), Scanning Electron Microscopy (SEM), High-Resolution Transmission Microscopy (HR-TEM), Brunauer-Emmett-Teller (BET) surface area analysis, Thermo-Gravimetric Analysis (TGA) and X-ray Photoelectron Spectroscopy (XPS). Gas sensing properties of undoped and doped samples were investigated by using the KENOSISTEC machine.

4.1 X-Ray diffraction (XRD)

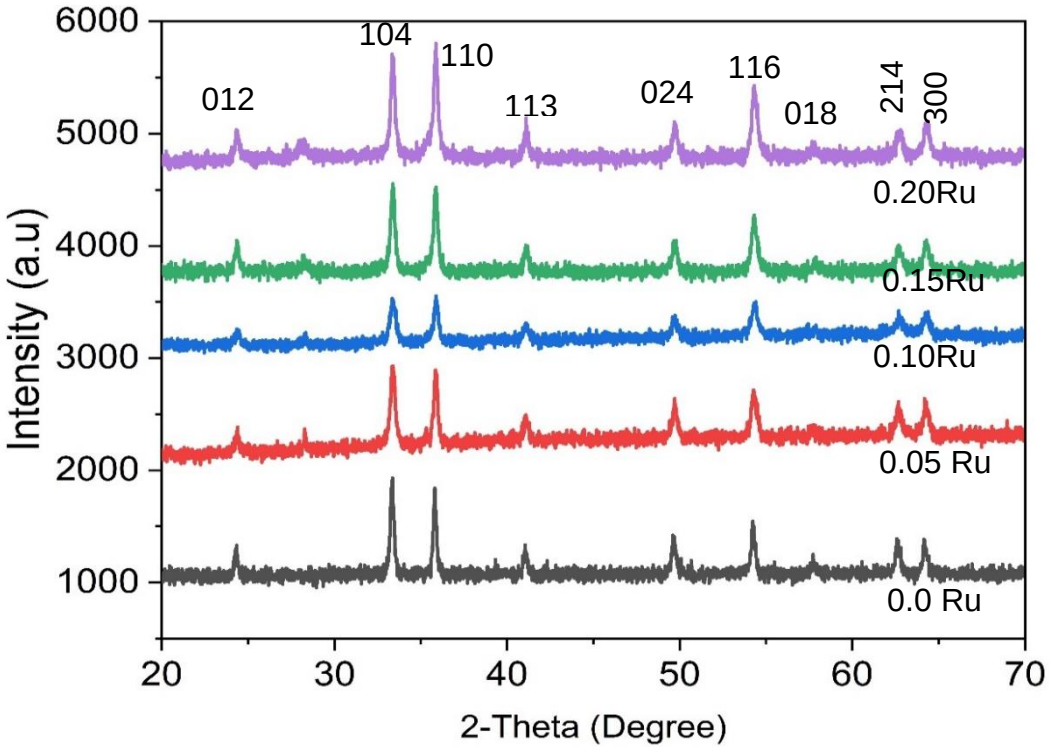

Figure 4.1: XRD results for undoped and doped samples with a different weight percentage of ruthenium.

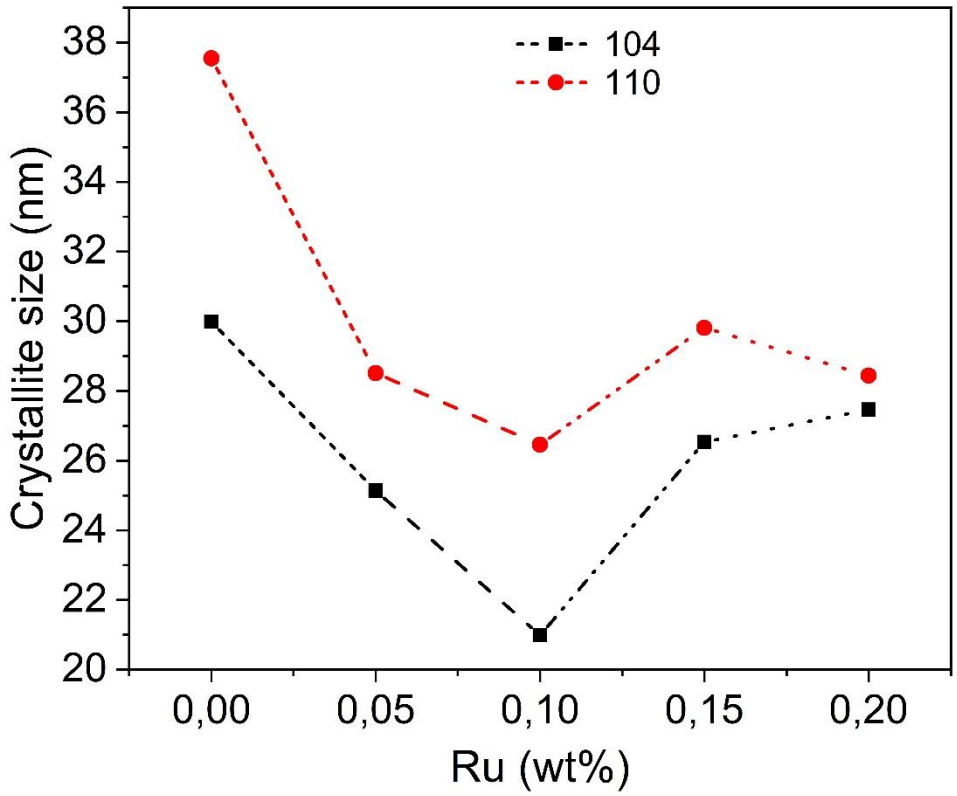

Figure 4.1.1: Plot of the average crystal size and the dopant concentration.

There were five samples used in this study, one of which was pure alpha iron oxide (α-Fe_2O_3) and the others were doped with various weight percentages of ruthenium ($RuCl_3$). To improve the sensitivity of alpha iron oxide, ruthenium was used as a dopant material in this study. **Fig. 4.1** shows the results of the XRD machine, which is available in the Department of Chemistry at UNIZULU. The X-ray diffraction pattern of the samples was determined using a German Bruker D8 PHASER X-ray diffraction system with Cu/K as the radiation source with the wavelength of (λ = 1.5418 Å), and data were collected in the range of 10 to 80 degrees at a scanning speed of 0.5, which is equivalent to 45 minutes per sample.

Fig. 4.1 shows nine peaks that appear in the following 2θ ranges: 24.37, 33.38, 35.86, 41.07, 49.58, 54.27, 57.92, 62.5,3 and 64.12 which correspond to the following planes :(012), (104), (110), (113) (024), (116), (018), (214), and (300) **[1-4]**.Only five of the strongest peaks are found in hematite (α-Fe_2O_3), according to a review of the literature. These include (012), (104), (110), (116), and (300). Other peaks, such as (113), and

(024), are weaker or have lower intensity, indicating the existence of hematite, which has rhombohedra (hexagonal) structures with lattice parameters of a = 0.5036 nm and c = 1.3749 **[5] [6-8]**. When have 0.05 wt % Ru, the second phase (RuO_2) starts to develop, and it increases with an increase with (wt %) of Ru as shown in **Fig. 4.1** with the red spot and this peak has the miller index of (110) which correspond 28.267 to following value of the 2-theta **[9, 10]**. The broadening line of this peak increases with the weight percentage of ruthenium.

The use of the different (wt%) of Ru changes the orientation of the peaks, their position, and broadening of the peaks. This is shown when we have 0.20 wt% Ru. The alpha iron oxide undoped shows that the most intense peaks are (104) and (110). And this normally indicates that the (α-Fe_2O_3-Ru) is growing more along the plane in that direction. The XRD results show the strongest peaks for all samples, which means the material has a highly polycrystalline structure. Ru-doped samples showed themselves to be unsuitable to be used as the dopant material to increase the sensitivity of alpha iron oxide.

Only the crystal size of the material affects the broadening of the lines in the XRD peaks. The average crystalline size associated with the XRD ranges between 24 and 34 nm.

$$D = \frac{k\lambda}{\beta cos\theta_B} \qquad (4.1)$$

where D is the crystalline size, K is the constant which is a constant number (0.9), λ is the wavelengths (0.1548 nm) and β is the full-width-half-maximum (FWHM) (in radians), and B on $\cos\theta_B$ is the angle at which the peak of the signal occurs. **Table 4** shows the particle size of different synthesised samples. The concentration decreases while the wt % of Ru is increasing, and the particle size is affected, while the α-Fe_2O_3 (undoped) showing a high particle size of 37.55 nm compared to the doped samples.

Table 4: Crystalline size calculated by using the Scherer equation above.

Samples	***(hkl)***	**2θ theta**	**FWHW**	**D(nm)**
Pure	(104)	33.33	0.28	29.99
	(110)	35.81	0.22	37.55
0.05 wt% Ru	(104)	33.38	0.33	25.13
	(110)	35.86	0.29	28.51
0.10 wt% Ru	(104)	33.38	0.39	20.99
	(110)	35.88	0.32	26.46
0.15 wt% Ru	(104)	33.37	0.31	26.53
	(110)	35.86	0.28	29.81
0.20 wt% Ru	(104)	33.37	0.30	27.46
	(110)	35.86	0.29	28.43

All sample peaks, (104) and (110) were analysed by using **Eq 4.1** and the crystalline size for all peaks gradually decreased referring to **Table 5**. Average particles size of all samples used in this study is also give on the table 5. If the concentration of the samples (undoped and doped Ru) decreased, it also caused the average particle size of all samples to change.

Table 5: Particle size of different synthesised samples (undoped and doped Ru).

Weight of $FeCl_3$(g)	**Weight of $Rucl_3$(g)**	**Samples**	**Concentration**	**Particle size**
1.622	0.0	α-Fe_2O_3	0.01M	34
1.422	0.05	α-Fe_2O_3-Ru	0.0993M	27
1.222	0.10	α-Fe_2O_3-Ru	0.0938M	24
1.022	0.15	α-Fe_2O_3-Ru	0.0907M	28
0.822	0.20	α-Fe_2O_3-Ru	0.0876M	28

4.2 Scanning Electron Microscopy (SEM)

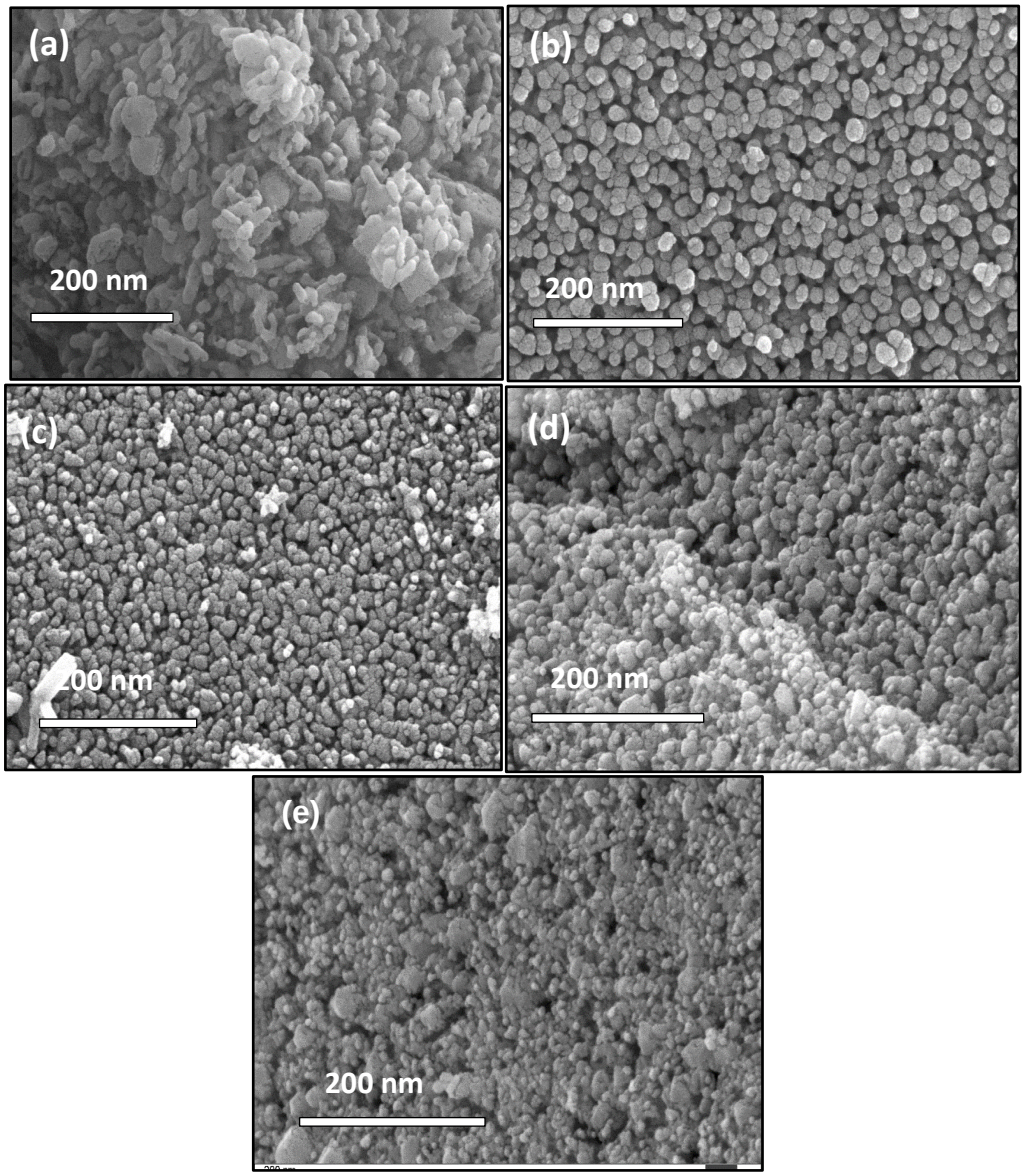

Figure 4.2: SEM images of (a) pure α-Fe_2O_3, (b) 0.05 wt% Ru, (c) 0.10 wt% Ru, (d) 0.15 wt% Ru, and (e) 0.20 wt% Ru.

The surface morphology of pure alpha iron oxide and ruthenium doped samples is shown on Fig 4.2(a) Nan rods (b-c) Porous spheres (d-e) porous spheres-with distorted cubes. The surface morphologies of each sample prepared were studied by using scanning electron microscopy (SEM). The surface layer of the sensing material must have a large surface number to enhance gas adsorption. And this can only be obtained if the material consists of the nanostructures such as Nanowires, Nan rods, and Nanoparticles. The surface morphology of the dopant samples depends on the concentration of the dopant material. At the high concentration, the surface

morphology of the material is still porous spheres but there is the formation of distorted stores. The second phase of the ruthenium starts when the dopant concentration is 0.15wt % Ru as shown in **Fig. 4.2(d)**, and it is seen as being white in colour in **Fig 4.2 (e)**.

4.3 High-Resolution Transmission Electron Microscopy (HR-TEM)

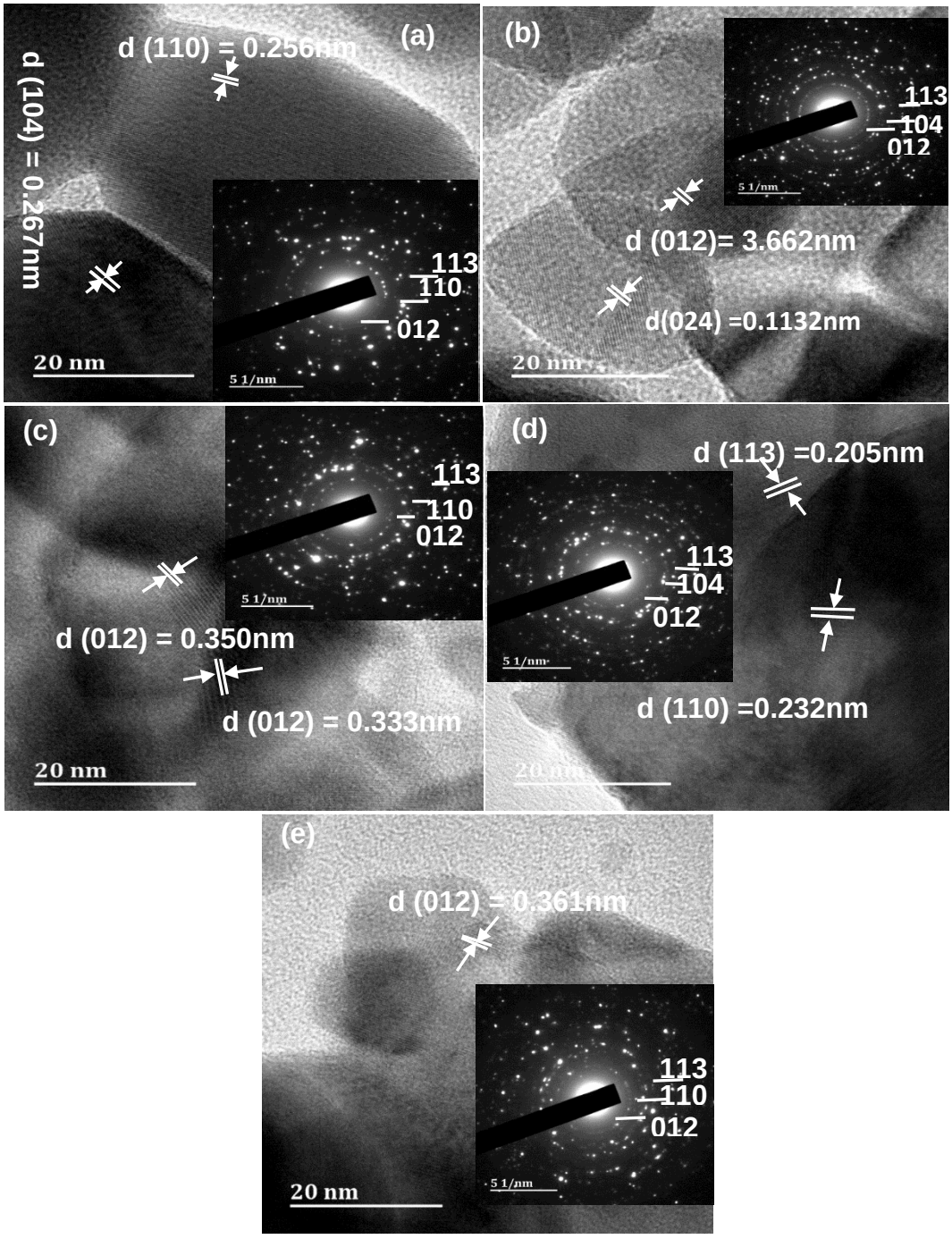

Figure 4.3 The result of High-resolution Transmission electron microscopy (HR-TEM) (a) alpha iron oxide, and doped samples with ruthenium at different weight percentages (b) 0.05 wt% Ru, (c) 0.10 wt% Ru, (d) 0.15 wt% Ru, and 0.20 wt% Ru.

The interplane distance of the fringes line is observed in the pure alpha iron oxide as shown in **Fig. 4.3(a)**, (104) corresponding to 0.267 nm, and (110) corresponding to 0.256 nm. However, for the doped samples, we have this (012) corresponding to 3.662 nm for 0.05 wt% Ru, (012) corresponding to 0.333 nm for 0.10 wt% Ru, (110) corresponding to 0.232 nm for 0.15 wt% Ru and (012) corresponding to 0.361nm. For each sample, there is a unique pattern of fringes line. (See **Fig. 4.3**), a selected area electron diffraction pattern (SAED) corresponding to HRTEM images of each sample is shown. To demonstrate polycrystalline material, SAED is inserted. Accordingly, HR-TEM images confirm the XRD result. The peaks are generally observed in areas where the material is growing **[11] [12, 13]**.

4.4 Brunauer-Emmett-Teller (BET)

The samples were analysed by using nitrogen adsorption at the temperature of 77.0 K, and the instrument used was micromerities. Before analysis of the samples, we degassed under the vacuum at a temperature of 150° C for 4hr. For the analysis, the instrumental parameter “equilibration time “was set to 15 s. BET theory aims to explain the physical adsorption of the molecules on the surface of the material and also serves as the basis for important analysis techniques to measure the specific area of the material and also to calculate the pore volume of the material.

The Nitrogen-adsorption-desorption isotherm of pure alpha iron oxide and ruthenium doped samples **(Fig. 4.4 (a-e))** is off type 5 according to the IPUAC classification and if (P/Po) is (0.8 -1.0) it indicates that the product has a typical mesoporous structure **[13]**. **Fig. 4.4 (a)** shows that pure samples of alpha iron oxide have high desorption while the absorption is low, See **Fig. 4.4 (b-e)** for the doped samples with a different weight percentage of ruthenium. Desorption is defined as the physical process where a substance is being released from the surface of the material. All doped samples show that desorption of the gas is much high while the absorption is lower. This is caused by an increase in the concentration of the dopant material. This procedure consists of scanning electron microscopy SEM images that show particle size and formation of the cube's distorted stone; therefore, the absorption of the gas is low.

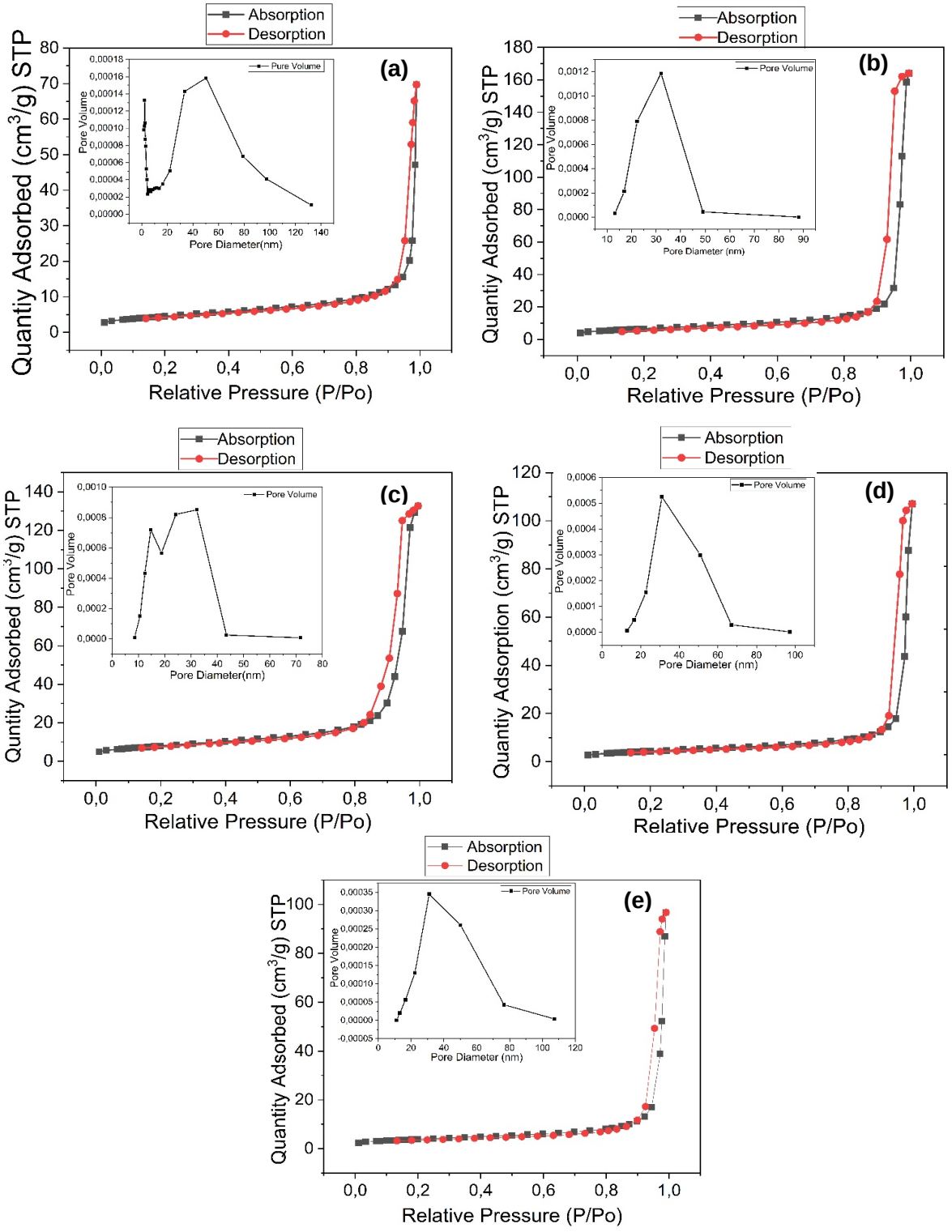

Figure 4.4: N_2 Adsorption-desorption isotherm curves of alpha iron oxide doped with ruthenium (a) alpha iron oxide, (b) 0.05 wt% Ru, (c) 0.10 wt% Ru, (d) 0.15 wt% Ru and (e) 0.20 wt% Ru doped samples and their corresponding pore size distribution plots for the as prepared samples in the inset.

4.5 Thermogravimetric Analysis (TGA)

The thermal stability of pure alpha iron oxide and ruthenium doped samples was evaluated by thermogravimetric analysis. There are a variety of atmospheres in which the thermal reaction occurs, including ambient air, vacuum, and inert gases. In this work, however, the result shows that the mass of the samples increased. This was because the samples were rained under air conditions. Thermal stability is when there is no change in mass. As a result, this material is not thermally stable. There are three types of TGA: Isothermal or static thermogravimetry, Quasistatic thermogravimetry, and Dynamic thermogravimetry. Quasistatic thermogravimetry was used for this research. The data sheet shows that the temperature was being raised sequentially by 10 ^{0}C per minute. Weight changes are monitored as a function of temperature or time during controlled temperature programs in controlled environments **[14]**. A pure alpha iron oxide sample is shown in **Fig. 4.5(a).** While the samples doped with ruthenium is shown in the **Fig. 4.5(b-e).** By the observation the increase in the dopant concertation it affects the stability of the material.

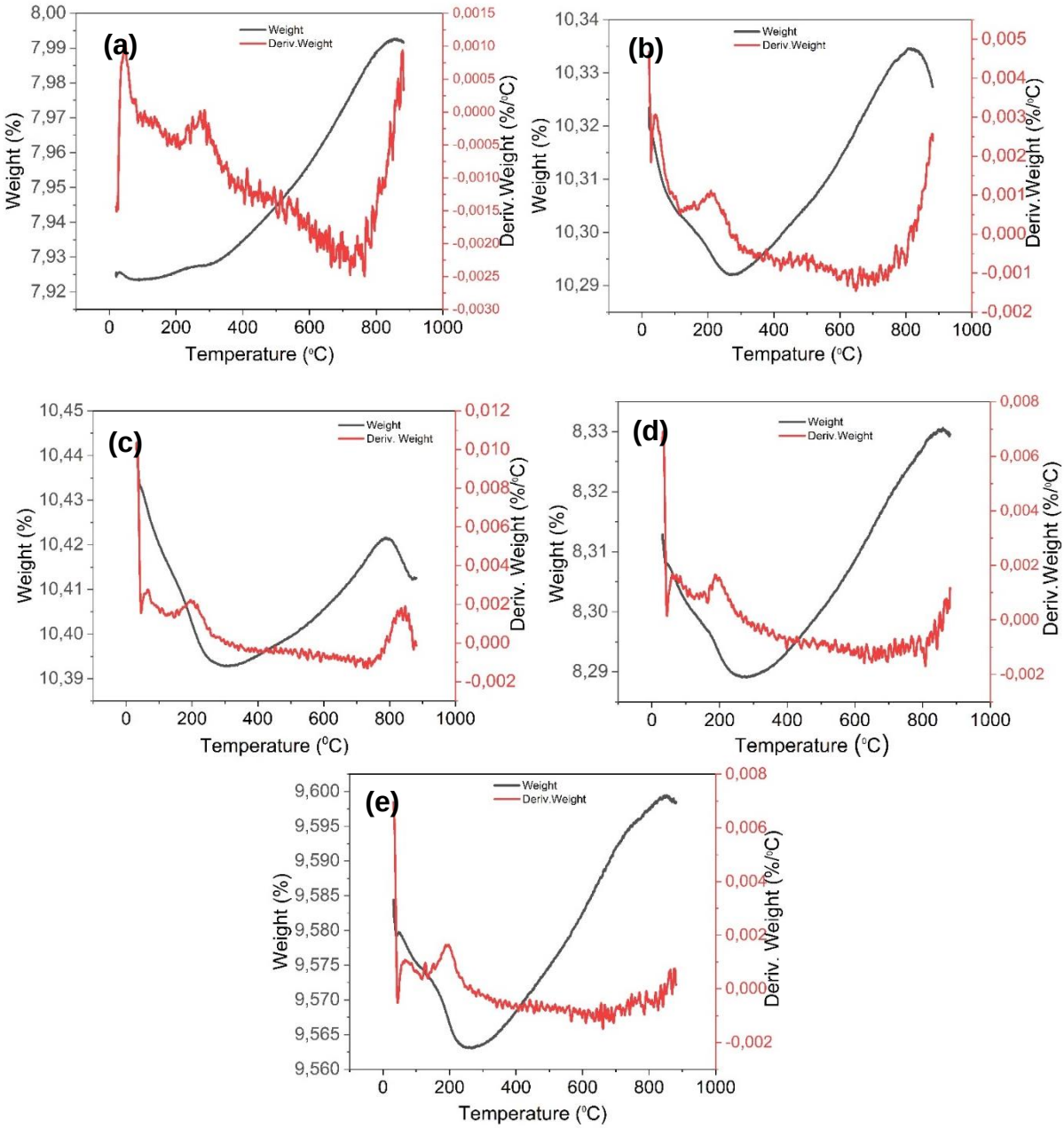

Figure 4.5: The results of TGA for pure and doped samples, (a) Alpha iron oxide, (b) 0.05 wt% Ru (c) 0.10 wt% Ru, (d) 0.15 wt% Ru and (e) 0.20 wt% Ru.

4.6 X-ray Photoelectron Spectroscopy (XPS)

X-ray photoelectron measurements were carried out to better understand the material's surface and chemical makeup. The PHI 5000 Scanning (ESCA) microprobe system was used. The samples were radiated by monochromatic Al K_α X-rays with the energy of 1486.6 eV and power of 25 W with a spot size of 100 um at the pressure of $1.4x10^{-8}$ Torr. The sample of pure alpha iron oxide (α-Fe_2O_3), and samples doped with different weight parentages were measured for XPS. Both samples of pure alpha iron oxide and samples that had been doped with ruthenium underwent survey scans. In particular, the survey demonstrates the elements found in the materials depicted in **(Fig. 4.6.1 and 4.6.2)**. But most importantly it confirmed the presence of Fe, O, and Ru in the materials. The narrow scan was done on both samples, pure and doped **[15-17].**

F**ig. 4.6.1** shows the XPS result for alpha iron oxide pure (α-Fe_2O_3). The survey scan shows three elements present in the sample of alpha iron oxide, namely, O1s, Fe2p, and Ru3d as shown in **Fig. 4.6.1 (a)**, Then each element was further investigated by XPS to confirm the binding energy of each this presented in **Fig. 4.6.1 (b-d)**. The Fe2p scan in **Fig.4.61 (b)** shows only three peaks that correspond to the following binding energy, respectively 710.1 eV, 711.5 eV, and 725.1 eV. The high peaks occur when the binding energy is lower, at 710.1 eV. The scan for O1s and Ru3d is shown in **Fig.4.6.1 (c-d)**) shows only two peaks, but for the O1s high peaks occur at the lower binding energy of 530.0 eV. For the Ru3d the high peak occurs when the binding energy is high, at 285.1 eV.

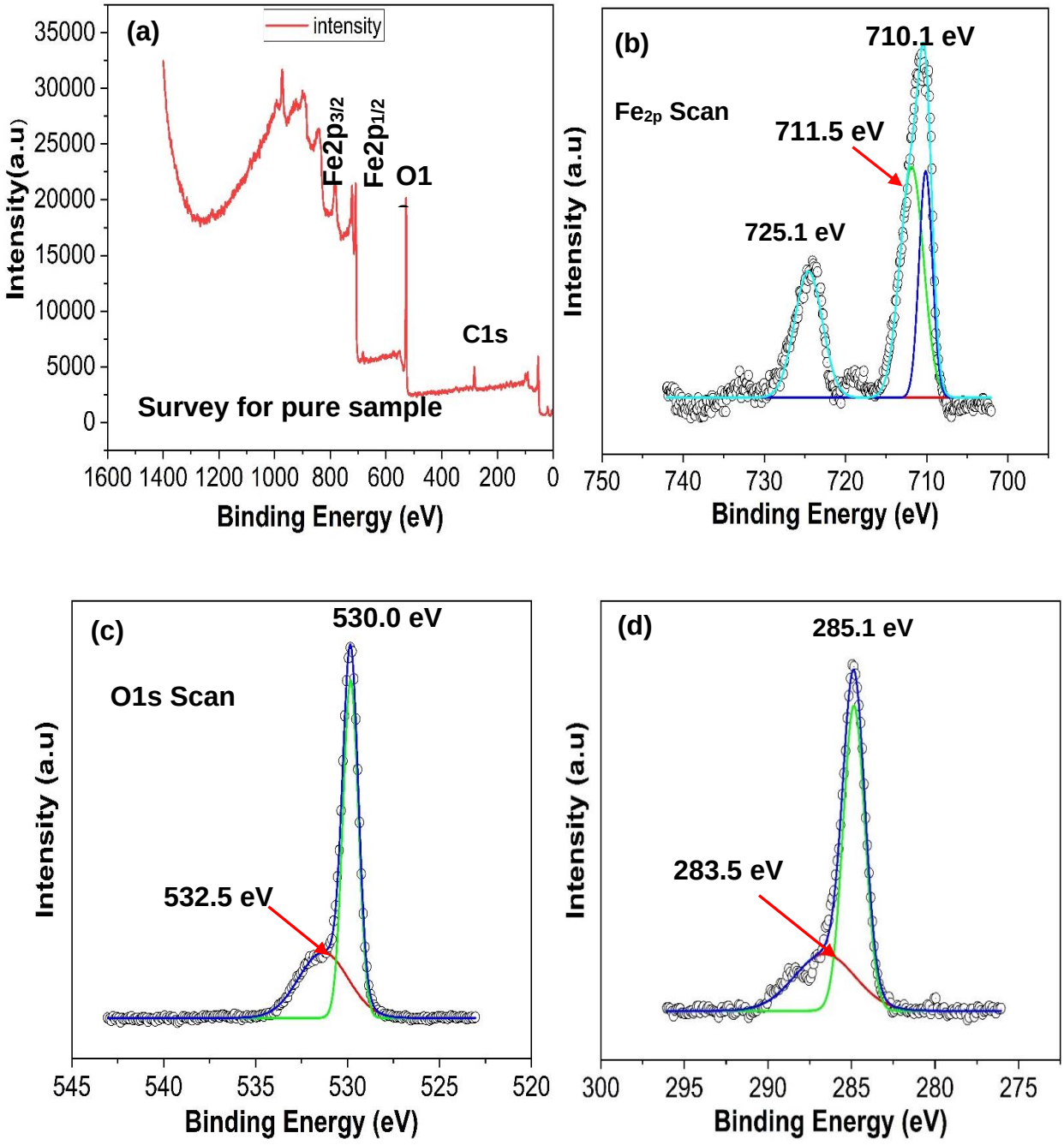

Figure 4.6.1: XPS result for the pure sample.

Fig. 4.6.2 below presents the measurement result of the XPS for the sample doped with 0.05 wt % Ru. The survey scan for all samples doped with ruthenium is given in **Fig. 4.6.2 (a).** Doped samples with 0.05 wt % Ru show only three scans, which are Fe2p, O1s, and Ru3d. This is presented in **Fig. 4.6.2** (**b-d)**. The scan Fe2p of the doped sample shows only three peaks, corresponding to binding energy 712.1 eV, 715.0 eV, and 725.1 eV. The high peaks occur at the lower binding energy of 712.1 eV, as shown in **Fig.4.6.2 (b)**. Comparing this with the Fe2p for pure sample shows

that the addition of dopant material affects the position of the peaks as well as the broadening of the peaks. The O1s scan shows only two peaks, which correspond to binding energy 529.4 eV and 532.5 eV (see **Fig.4.6.2 (c)**). The Ru3d scan for the doped sample shows only three peaks, corresponding to the following binding energy: 292.4 eV, 285.2 eV, and 283.3 eV. By comparing it to pure Ru3d it shows that if the binding energy is 285.2 eV. The development of the new peak could have been caused by the addition of the dopant material on the samples as shown in **Fig.4.6.2 (d)**).

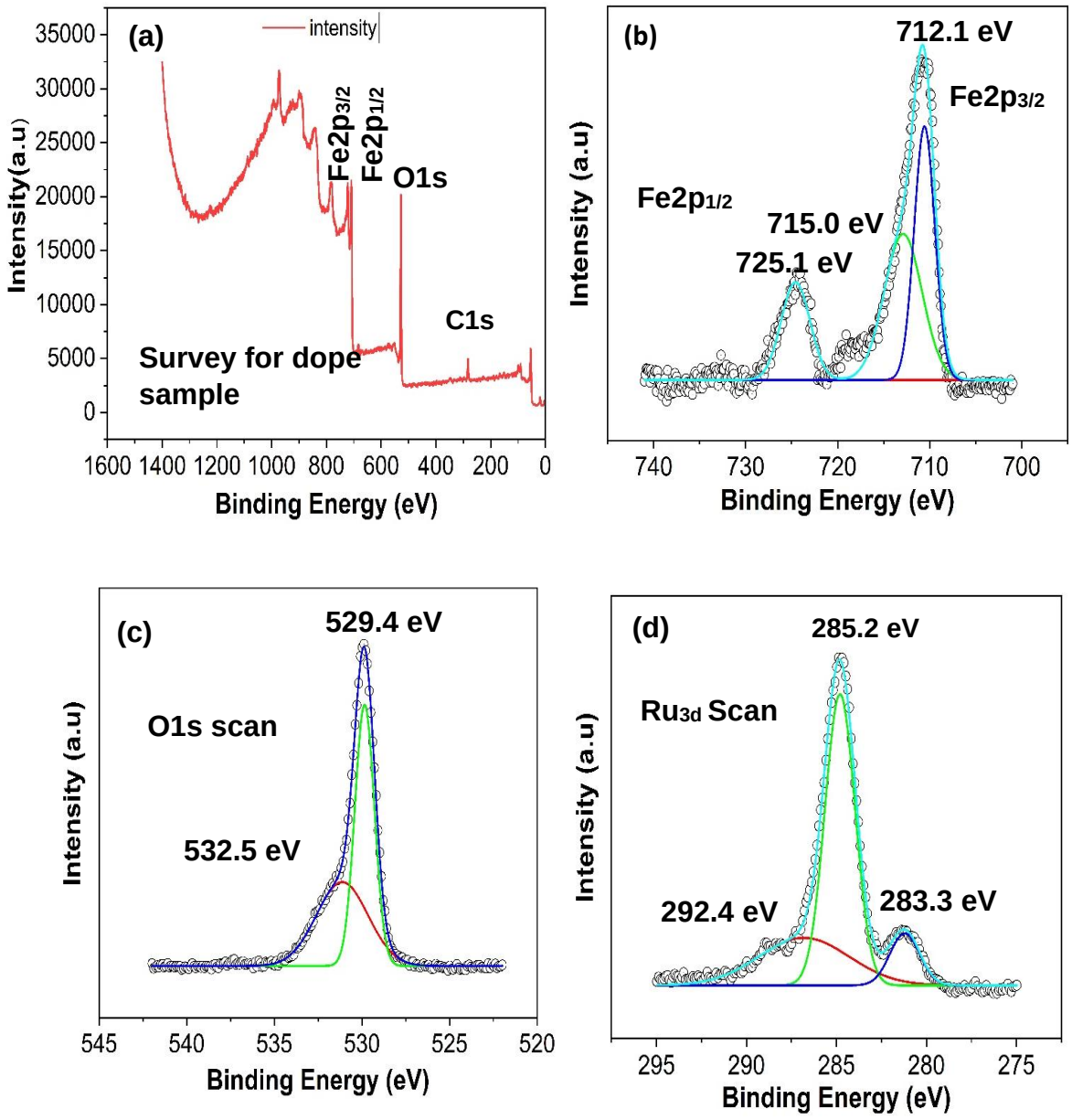

Figure 4.6.2: XPS results of the sample doped with 0.05 wt % Ru.

Fig. 4.6.3 shows the three scans of Fe2p, O1s, and Ru3d of the element present in the sample. As the dopant weight increases, it also affects the formation of the peaks, and their broadening and height. The Fe2p scan shows only three peaks, corresponding to the binding energy of 725.0ev, 711.3 eV, and 719.5 eV. The high peaks occur at the lower energy of 711.3 eV. When the binding energy is 719.5 eV, this mean that new peaks has developed and, by comparing with the Fe2p scan of the pure sample as shown in **Fig. 4.6.3 (a)** below. The O1s scan shows only two peaks that are more like O1s for the pure sample see **Fig. 4.6.3 (b)**. However, the Ru3d scan shows only three peaks with high height compared to the pure sample see **Fig. 4.6.3 (c)**.

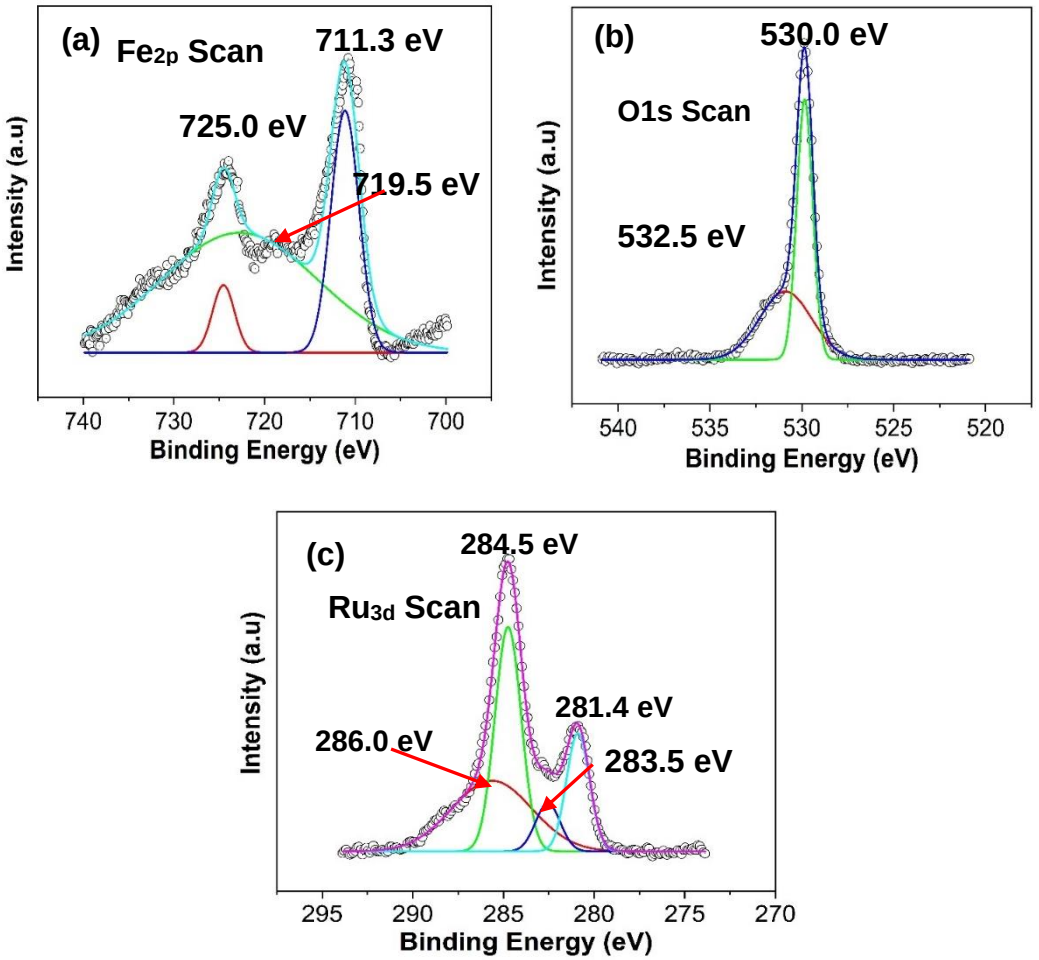

Figure 4.6.3 XPS results of the sample doped with 0.10 wt% Ru.

Fig. 4.6.4 shows three scans for the sample doped with 0.15 wt% Ru, namely Fe2p, O1s, and Ru3d respectively. In **Fig. 4.6.4 (a)** the Fe2p scan shows only four peaks on the following binding energy 732.1 eV, 725.0 eV, 718.1 eV, and 710.0 eV. Comparing this to the Fe2p for the 0.15 wt% Ru we have developed a new peak while the binding energy is 732.1 eV, and the highest peak occurs at 710.0 eV. Below is the scan of O1s (see **Fig. 4.6.4 (b)**), It shows only two peaks corresponding to 532.5 eV and 529.5 eV, while the highest peaks occur when the binding energy is lower. The scan for Ru3d shows only four peaks, corresponding to the binding energy of 289.1 eV, 285.1 eV, 284.0 eV, and 283.0 eV. A new peak has been developed when the binding energy is 284.0 eV as shown in **Fig. 4.6.4 (c)** below.

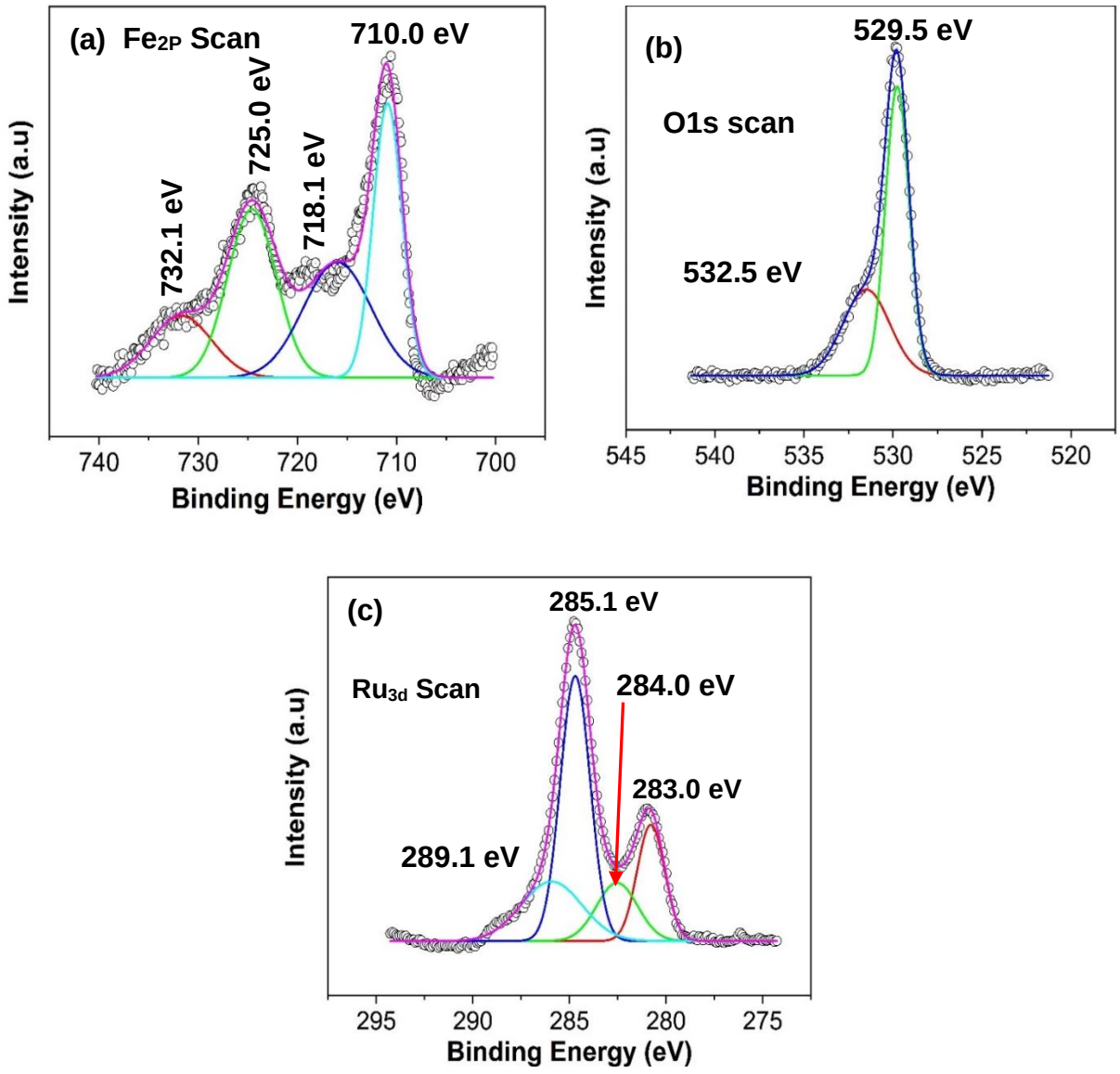

Figure 4.6.4: XPS results for the sample doped at 0.15 wt% Ru.

Fig. 4.6.5 shows the scans Fe2p, O1s, and Ru3d of the sample doped with 0.20 wt% Ru. The Fe2p scan see **Fig. 4.6.5(a)** consists of three peaks, which correspond to the binding energy 725.0 eV, 715.0 eV, and 713,2 eV. The highest peaks occur when the binding energy is 713.2 eV. The spreading of the peaks is affected by the increase in the concentration of impurity added to the sample. The O1s scan see **Fig. 4.6.5 (b)** consists of two peaks, corresponding to the binding energy 530.0 eV and 532.5 eV. Finally, the scan of Ru3d shows only three peaks, with the highest peak occurring at the high binding energy of 285.1 eV as shown in **Fig. 4.6.5 (c)**.

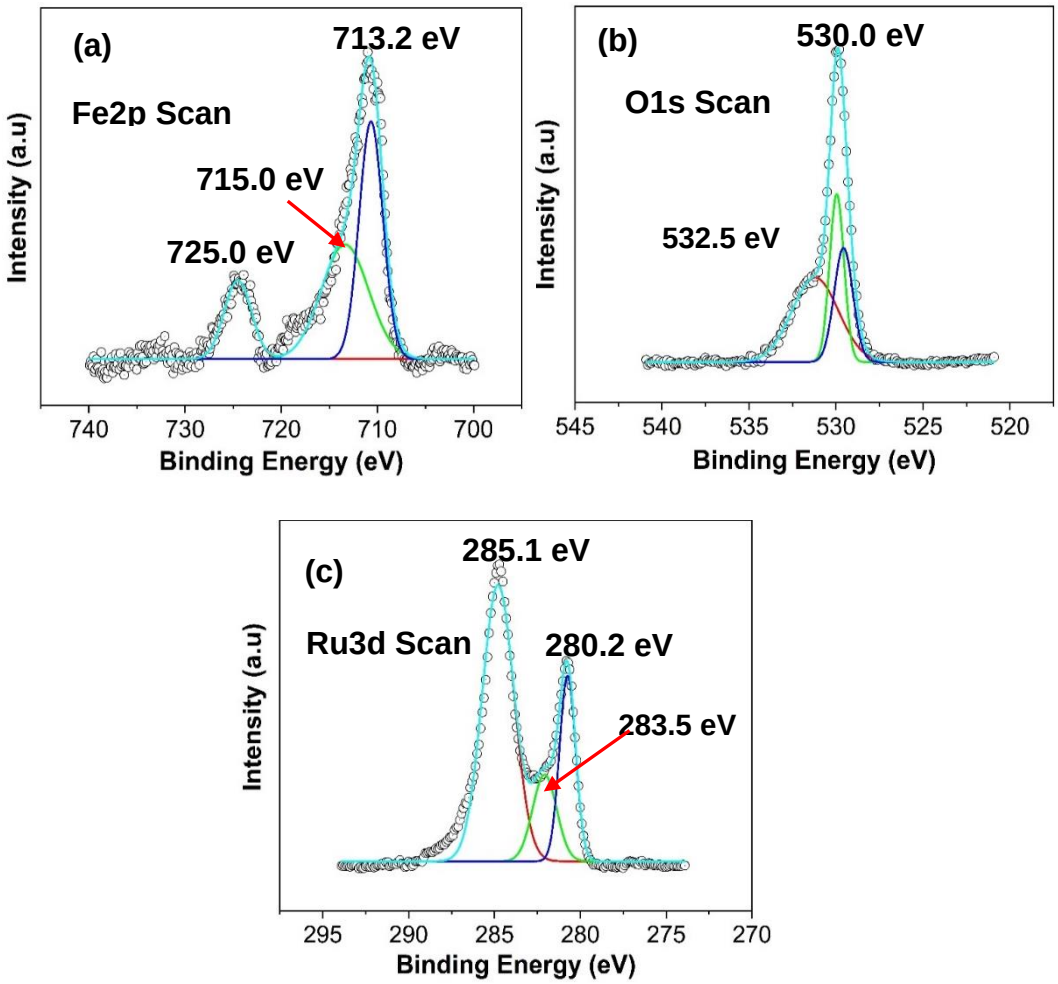

Figure 4.6.5: Results from the XPS sample doped at 0.20 wt% Ru.

4.7 Gas sensing Measurement

To study the gas sensing properties of alpha iron oxide and ruthenium doped, samples were sonicated for 2hr in the ultra-sonicate bath. After that the drop-casting method was used to drop the samples on the substrate pre-printed with the platinum electrode on the top. The sensor was allowed to dry to remove the organic residual at the temperature of 120 ºC.

The gas sensing measurement was conducted using a KS026K16 (KENOSISTES model of the 2016 year). The samples of different weight percentages of ruthenium were placed inside the chamber on the systems electrical and gas feeds for sensing measurement. On the system, the temperature was set at 225 ºC, 200 ºC, and 175 ºC, while the voltage was set to 5.0 V across all the sensor measurements. The sensor was coated with silver metal contacts at the edges to create the ohmic contact. Liquefied petroleum gases (LPG), ammonium (NH_3), ethanol, and propanol were the target gases for this study. The concentration of the target gas for LPG was (1k ppm-10k ppm) at a high temperature of 225 ºC and (200, 400,500, 600,800, 1000, 1500, 2000, 2000, and 2000) ppm at an operating temperature of 200 ºC, but for the other targets, the concentration was (5, 10, 20,40,60,80, and 100) ppm.

The gas in the system was pushed with dry air or synthetic air which is (79% and 21%) to dilute conduct the measurement. Before the gas was introduced into the chamber, dry air was used to flush the chamber for 30 minutes to reach a state of equilibrium Then the target gas was introduced into the chamber for 10 minutes, after which dry air was introduced again, but this time for 10 minutes, which allowed the samples to recover. This was done for concentration in all gas sensing measurements. The Keithley 6487/E pico ammeter/ voltage source was used to quantify the current of the sensor. Then, to calculate the electric gas response (S) of the sensor, the following equation was used, where I_g and I_a represent the current in the air and the presence of the target gas:

$$S=\frac{Ig-Ia}{Ia} \qquad (4.2)$$

The response was calculated by using the above equation and recorded in **Table 6.**

Table 6: Calculated response to the different gases.

Samples	**Ethanol**	**Propanol**	**LPG**	**NH_3**	**H_2S**
Pure	7.680	12.410	24.410	26.01	9.281
0.05 wt% Ru	3.127	5.840	11.928	8.176	6.598
0.10 wt% Ru	0.928	1.251	5.988	2.517	1.846
0.15 wt% Ru	1.027	1.360	6.580	2.079	2.114
0.20 wt% Ru	1.291	1.291	2.531	0.754	0.875

Alpha iron oxide pure and ruthenium doped samples consisting of different weight percentages of ruthenium were exposed to different gases (ethanol, propanol, liquefied petroleum gases (LPG), ammonium, and hydrogen sulphide). Based on observation, the pure sample is the best sample as it has more selectivity in NH_3 gas and shows a higher response than the other samples. The weight of the impurity increases the selective shift to the LPG. See **Fig 4.7**.

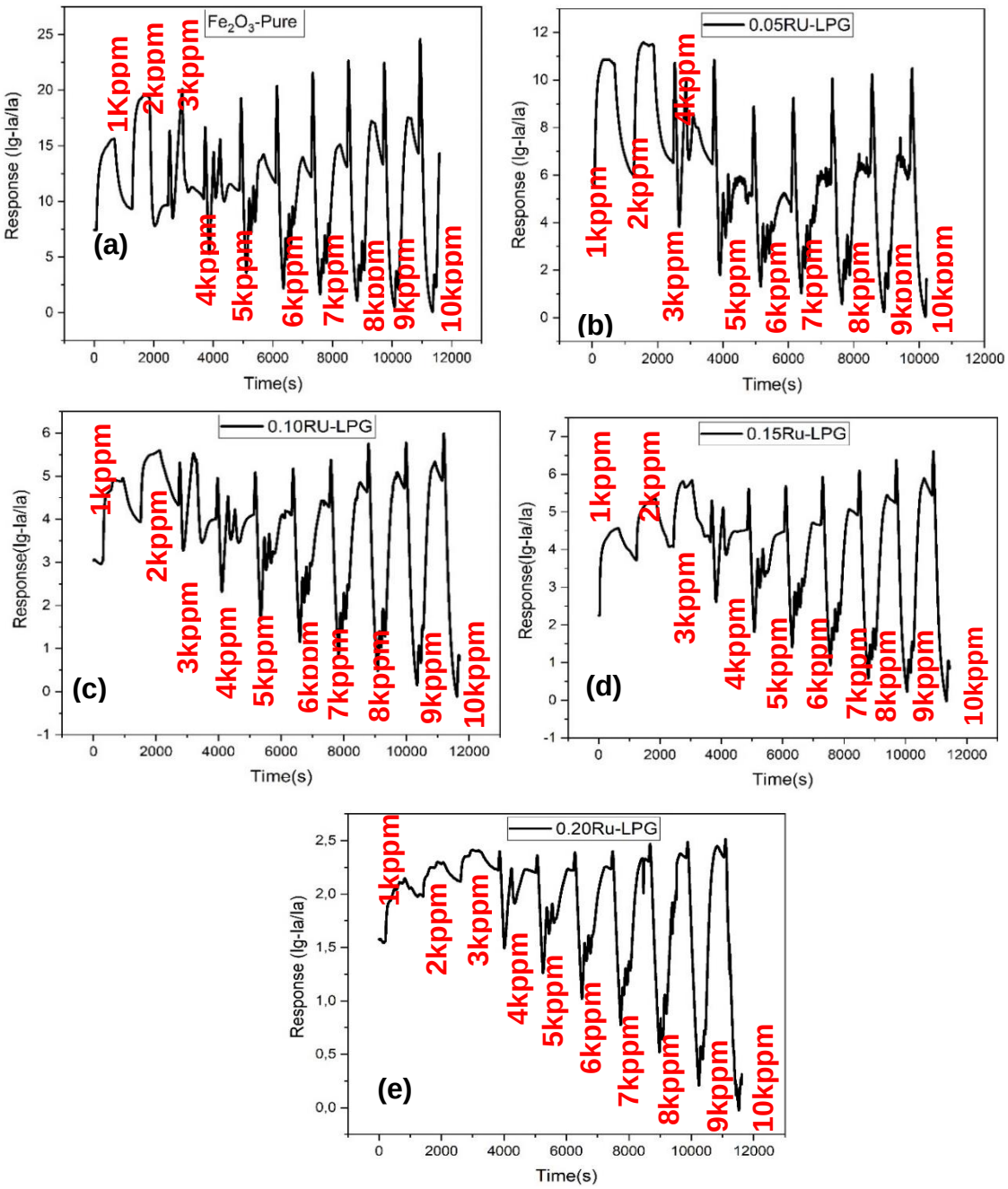

Figure 4.7: Response of pure samples and ruthenium doped samples towards LPG, (a) Alpha iron oxide, (b) 0.05 wt% Ru, (c) 0.10 wt% Ru, (d) 0.15 wt% Ru, and (e) 0.20 wt% Ru at an operating temperature of 225 ºC.

The focus of this study is based on the selectivity of pure samples of alpha iron oxide towards the liquefied petroleum gas (LPG) because it shows its transition from n-types to p-types at different operating temperatures. Ruthenium-doped samples were expected to increase the response of the pure alpha iron oxide; hence it does not improve the response of alpha iron oxide. But ruthenium has been used in other

studies for improving solar energy and splitting water. The calculated response in **Table 6** shows that the dopant is not good enough to increase the response on the sensor as the results show that it decreases for all doped samples. The data in **Table 6** were used to plot a comparison of alpha iron oxide and ruthenium-doped samples for different target gases at different concentrations.

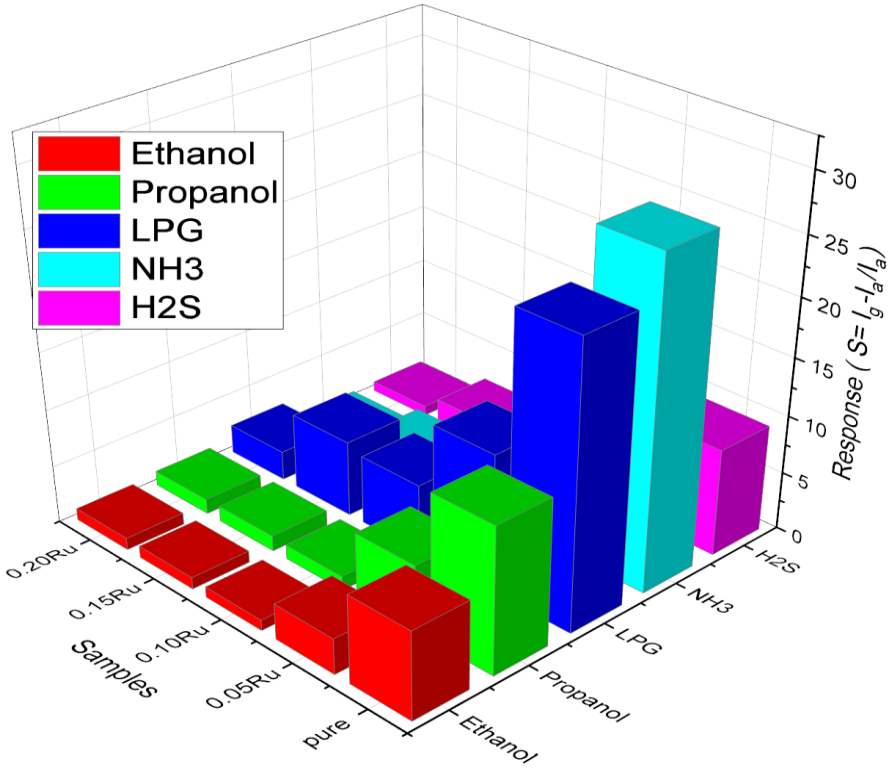

Figure 4.8: Selectivity comparison of alpha iron oxide doped with ruthenium for different target gases at different concentrations.

Pure alpha iron oxide is the best sample, and it is selective to ammonia. In this study, were more focused on the ruthenium-doped samples with various weight percentages. After doping we found that the response of NH_3 decreases with the increase of the dopant material. By comparing the liquefied petroleum gas (LPG) and NH_3 response from (0.05 to 0.20 wt% Ru) we found that pure samples it the best sample and it more selective to the LPG this is shown in see **Fig 4.9**.

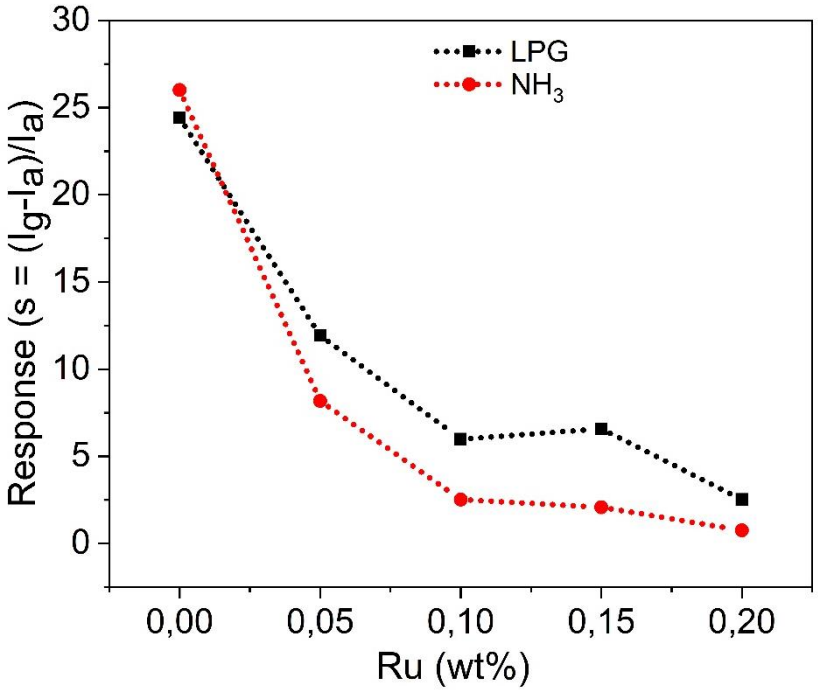

Figure 4.9: A comparison of liquefied petroleum gas (LPG) and NH_3 responses while the dopant concentration is increased.

4.7.1 Alpha iron oxide (Fe_2O_3) based sensor for the LPG

Pure alpha iron oxide is selective towards the LPG. The resistance of the sensor increased to reach certain values and then dropped down to the original resistance once the LPG was turned off this is normal base on previous studies. α-Fe_2O_3 is the n-type semiconductor since the resistance increases while the current is decreasing, and this type of behaviour satisfies Ig/Ia while Ig and Ia current is in the air and present in the target gas. This means that α-Fe_2O_3 is the oxidising gas in this case. But as the concentration of the target gas (LPG) increases alpha iron oxide starts to transform into a p-type semiconductor, which implies that α-Fe_2O_3 at high concentration is reducing the gas. Normally this transformation depends on the factors of temperature and concentration of the target gases.

The system was set to operate with a temperature of 225 ºC for all samples and the sensor response of pure alpha iron oxide and ruthenium doped shows ten cycles of LPG concentration from 1k ppm to 10k ppm. From 1k ppm to 2k ppm the response is n-type. The transformation occurs at 3k ppm and from 4kppm to 10kppm we have the p-type see **Fig. 4.10 (a)**.

Then the operating temperature was changed to 200 ºC and 175 ºC. If the temperature is 200 ºC there is a delay in the formation of the transformation, in this case from 1k ppm to 5k ppm, we have n-type. The transformation starts at 6k ppm of LPG gas and from 7k ppm to 10k ppm we have the p-type material. By further decreasing the operating temperature to 175 ºC we note the position at which the transformation occurs is at 10 k ppm while the concentration of liquefied petroleum gas (LPG) ranges between 1k ppm to 9kppm, and this simple mean that we have n-type material see **Fig. 4.9 (b-c).**

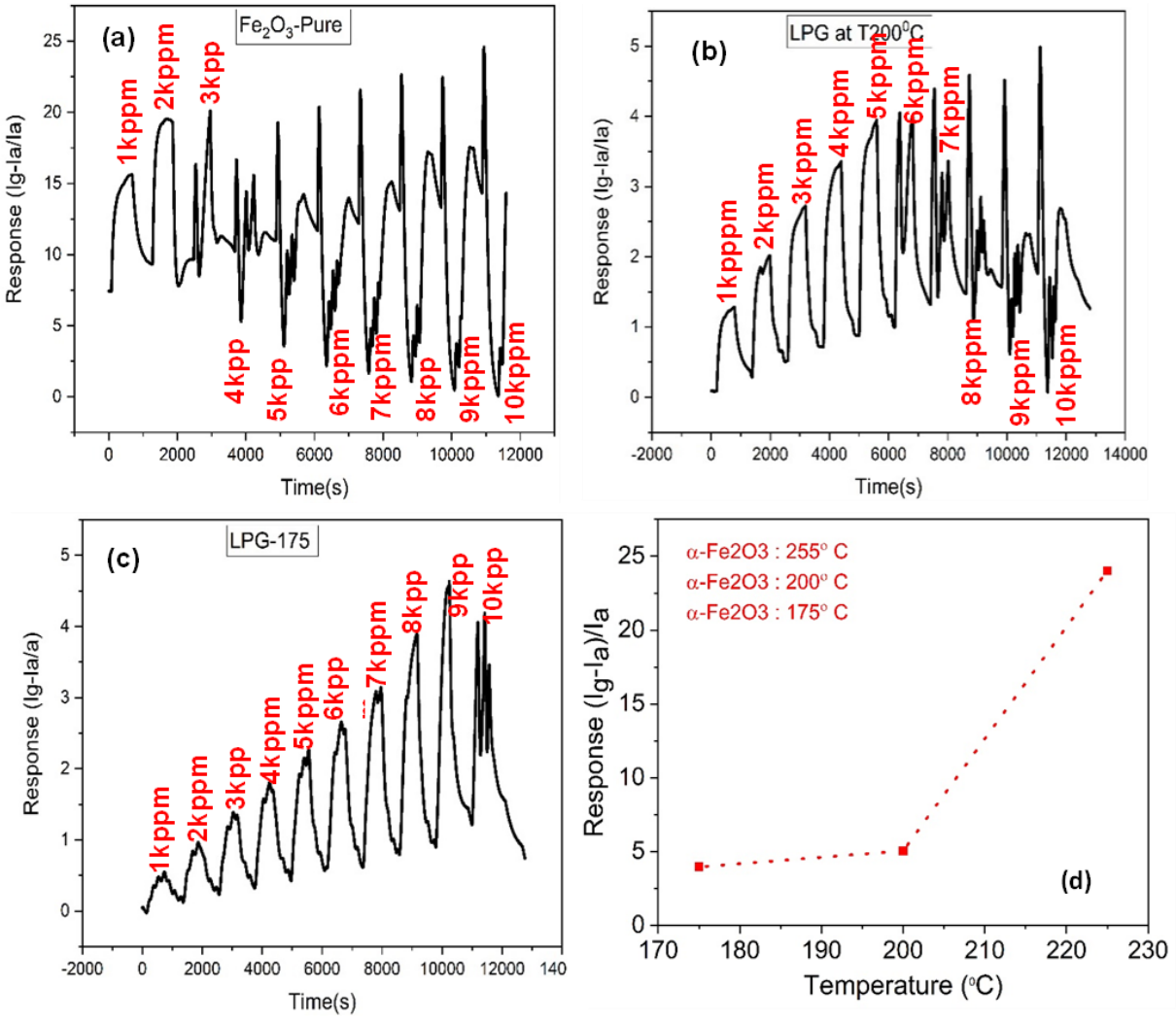

Figure 4.10: Response of alpha iron oxide towards LPG gas at different operating temperatures (a) 225 ºC, (b) 200 ºC, and (c) 175 ºC.

If the concentration of liquefied petroleum gas (LPG) is 2k ppm at high temperatures only two cycles show n-type and those cycles are facing up, see **Fig 4.10(a).** The sample of alpha iron oxide was tested on the different concentrations of LPG to validate that for any values of the concentration of LPG less than 2k ppm the material is n-type. These are values of the LPG concentration (200, 400, 500, 600, 800, 1k, 1.5k, and 2k) ppm **see Fig.4.11.**

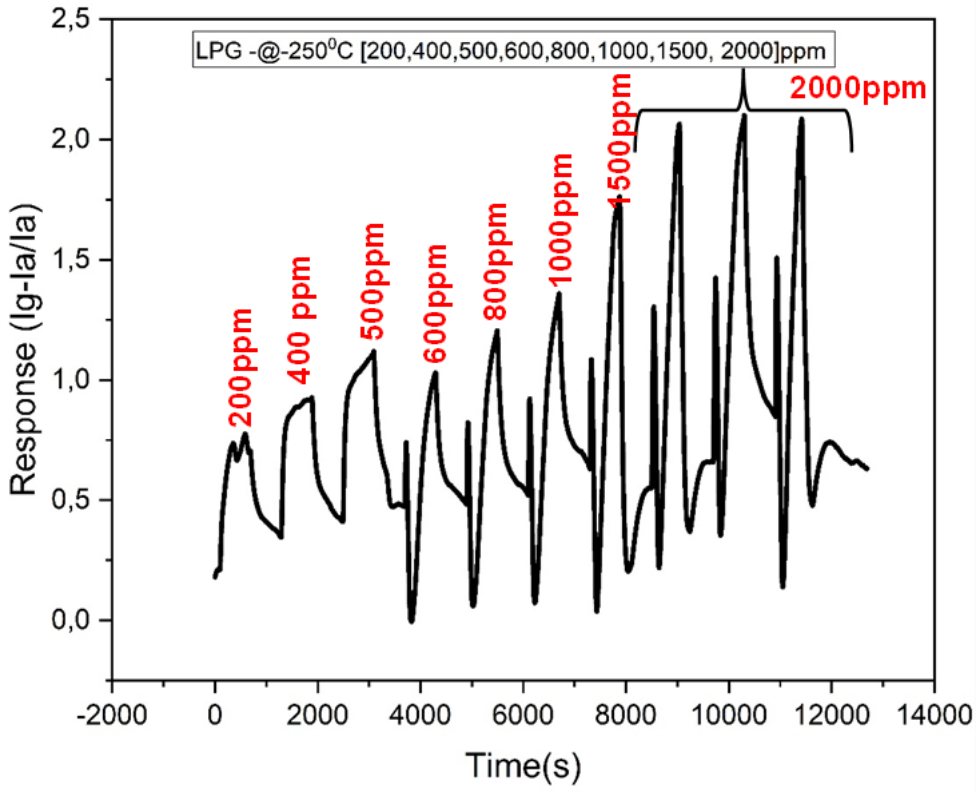

Figure 4.11 above shows that α-Fe_2O_3 is n-types for values less than 2k ppm at 225º C.

Reference

1. Cui, H., Y. Liu, and W. Ren, *Structure switch between α-Fe_2O_3, γ-Fe_2O_3 and Fe_3O_4 during the large scale and low temperature sol–gel synthesis of nearly monodispersed iron oxide nanoparticles.* Advanced Powder Technology, 2013. **24**(1): p. 93-97.
2. Lassoued, A., et al., *Control of the shape and size of iron oxide (α-Fe_2O_3) nanoparticles synthesized through the chemical precipitation method.* Results in physics, 2017. **7**: p. 3007-3015.
3. Synek, P., O. Jašek, and L. Zajíčková, *Study of microwave torch plasmachemical synthesis of iron oxide nanoparticles focused on the analysis of phase composition.* Plasma Chemistry and Plasma Processing, 2014. **34**(2): p. 327-341.
4. Takami, S., et al., *Hydrothermal synthesis of surface-modified iron oxide nanoparticles.* Materials Letters, 2007. **61**(26): p. 4769-4772.
5. Haider, S., et al., *Visible light active Cu-doped iron oxide for photocatalytic treatment of methylene blue.* Ceramics International, 2022. **48**(6): p. 7605-7612.
6. Lassoued, A., et al., *Synthesis, photoluminescence and Magnetic properties of iron oxide (α-Fe_2O_3) nanoparticles through precipitation or hydrothermal methods.* Physica E: Low-dimensional Systems and Nanostructures, 2018. **101**: p. 212-219.
7. Dehbi, A., et al., *Hematite iron oxide nanoparticles (α-Fe_2O_3): Synthesis and modelling adsorption of malachite green.* Journal of Environmental Chemical Engineering, 2020. **8**(1): p. 103394.
8. Kushwaha, P. and P. Chauhan, *Influence of different surfactants on morphological, structural, optical, and magnetic properties of α-Fe_2O_3 nanoparticles synthesized via co-precipitation method.* Applied Physics A, 2022. **128**(1): p. 1-14.
9. Al-Hajji, L., et al., *RuO_2 nanoparticles-accommodated graphitic carbon nitride for significant enhancement in photocatalytic oxidation of trichloroethylene.* Optical Materials, 2022. **125**: p. 112086.

10. Shimoyama, Y., et al., *RuO_2 Nanoparticle-Embedded Graphitic Carbon Nitride for Efficient Photocatalytic H_2 Evolution.* ACS Applied Nano Materials, 2021. **4**(11): p. 11700-11708.
11. Miser, D.E., et al., *HRTEM characterization of phase changes and the occurrence of maghemite during catalysis by an iron oxide.* Applied Catalysis A: General, 2004. **258**(1): p. 7-16.
12. Gandha, K., et al., *Mesoporous iron oxide nanowires: synthesis, magnetic and photocatalytic properties.* RSC advances, 2016. **6**(93): p. 90537-90546.
13. Farooq, N., et al., *Synthesis and characterization of clay graphene oxide iron oxide (clay/GO/Fe_2O_3)-nanocomposite for adsorptive removal of methylene blue dye from wastewater.* Inorganic Chemistry Communications, 2022. **145**: p. 109956.
14. Karaagac, O. and H. Köçkar, *Improvement of the saturation magnetization of peg coated superparamagnetic iron oxide nanoparticles.* Journal of Magnetism and Magnetic Materials, 2022. **551**: p. 169140.
15. Ni, Z., et al., *Performance and potential mechanism of transformation of polycyclic aromatic hydrocarbons (PAHs) on various iron oxides.* Journal of Hazardous Materials, 2021. **403**: p. 123993.
16. Devi, S., et al., *Phase transformation and structural evolution in iron oxide nanostructures.* Materials Science and Engineering: B, 2021. **272**: p. 115329.
17. Flak, D., et al., *In situ ambient pressure XPS observation of surface chemistry and electronic structure of α-Fe_2O_3 and γ-Fe_2O_3 nanoparticles.* Applied Surface Science, 2018. **455**: p. 1019-1028.

Chapter 5

5.1 Summary and Conclusion

The synthesis of pure alpha iron oxide and ruthenium doped was done by using the chemical-precipitation method. The samples were doped with a different weight percentage of ruthenium as follows (0.0, 0.05, 0.10, 0.15, and 0.20) wt% Ru. Both samples, doped and undoped, underwent different characterisation techniques to study certain properties of the material. From the X-ray diffraction (XRD) result for the undoped sample, it was concluded that the alpha iron oxide is rhombohedra with five intensity peaks, (104) and (110), and with a crystal particle size of 34 nm. The XRD result for the doped is similar to undoped samples, but the peak (104) is being reduced while the peak (110) is being increased to become more dominant. An increase in the concentration of the dopant material leads to the formation of the second phase of ruthenium (RuO_2). The miller index of the second phase was found to be (110), which corresponds to a 28.267 value of 2-theta (Degree).

Scanning electron microscopy (SEM) images of alpha iron oxide show that it is nan rods. For the doped samples with a different weight percentage of ruthenium, the SEM image shows that an increase in the concentration of the dopant material affects the formation of the particles in the material. At high concentrations, the SEM image shows a porous sphere with small cubes on it, and the second phase (RuO_2) is present.

The surface area was studied by BET. The result for undoped has a large pore size. The doped sample shows that as the concentration of the dopant increased the pore size of the sample gradually decreased. These results are in line with the scanning electron microscopy (SEM) images.

To study the thermal stability of the material TGA was used. The result for undoped and doped samples shows an increase in the mass of the material. This implies that this material is not thermo-stable, and this had a huge impact on the gas-sensing performance of the material.

Alpha iron oxide has been used by many researchers because it shows good properties for gas sensing performance. Ruthenium has been used in other research, for example, water spiriting and solar energy. In the study, alpha iron oxide was doped

with a different weight percentage of ruthenium with the idea of increase the sensing properties of the material towards different flammable gases. The sensors were fabricated by using the drop-casting method and those sensors were subjected to highly flammable gases to test gas sensing performance at an operating temperature of 225 ºC. The sensors were subjected to the following gases, liquefied petroleum gas (LPG), Ammonia (NH_3), Ethanol, Propane, and hydrogen sulfide. The pure sample (α-Fe_2O_3) was more sensitive to the target gases, with the response being 26.01 towards NH_3, while the response decreased upon the addition of different-weight ruthenium to alpha iron oxide. The selectivity shifted towards the LPG see **Fig. 4.9**. Ruthenium was found to be unsuitable to be used as a dopant material in alpha iron oxide for gas sensing applications. Therefore, ruthenium can be also used as a dopant material in another field of study or with another material but not alpha iron oxide.

Detection of flammable, toxic gases is very important in many different fields such as industrial emission control, and household and social security. Metal oxide semiconductor (MOS) gas sensors are among the most utilised to detect a large variety of gases being present. Based on the results it was found that ruthenium is not a good dopant material to alpha iron oxide in the application of gas sensing. The results of the doped samples show gradual decreasing upon the addition the of the ruthenium in alpha iron oxide. This simple indicate that ruthenium is not good enough to use as the dopant material.

5.2 Recommendation

The combination of alpha iron oxide doped with ruthenium was found to be not good for gas sensing performance, meaning that ruthenium is unsuitable to be used as a dopant material in alpha iron oxide. Ruthenium has good properties in other applications such as water sprinting and solar energy. In the future, ruthenium can be used as a dopant with other materials, but not with alpha iron oxide.